

General Comments:

This work investigates the aerosol chemical composition in Harbin in the past 2 years based primarily on in-situ measurement. Generally, I find that this manuscript may be more like a measurement report since that it does not provide sufficient new insight into atmospheric chemistry but the dataset seems unique and presents some new perspectives. One main problem with this work is that it entirely attributed the variations of secondary aerosol to the chemical processes, but aerosol does have a lifetime of 1~2 weeks and regional transport could largely contribute to the temporal variation at one specific site. Overall, I think this work fits the scope of ACP but there are some issues that need to be addressed to improve this work.

Our responses: We thank the referee for the constructive comments. The referee raised one major point regarding the roles of meteorology and regional transport, and further expanded in the specific comment #2. Please refer to our responses to that specific comment #2 for details.

Major Comments:

(1) The method ought to be detailed in the main text. Section 2 is too sketchy, in which some basic information like the geographic location of the campaign site, its representativeness, the main emission sources in the surrounding areas, the instrumentation and the QAQC should be included. Also, other analysis like AWC, Positive Matrix Factorization (PMF) results discussed in Section 3, which is not from the direct observation, should be described in this section. This article itself missed a lot of necessary information on the method and analysis tools. I suggest moving the supplementary method to the main text. Another issue related to the method is that PMF analysis usually needs a large amount of data to support the factorizations since that it basically is statistical analysis. According to the Supporting Information, the sampling number is around 200~300, which is not enough to get a reliable result.

Our responses: Two points were raised in this comment. The first one was that the Methods section (i.e., Section 2) should be expanded substantially, by including all the necessary information. Following this suggestion, (i) detailed descriptions of the filed campaign, which was originally presented as supplementary information, was moved to the main manuscript, and (ii) procedures of the ISOROPPIA and PMF analyses were

also moved to the Methods section. In the revised manuscript, Section 2 was re-organized as:

2.1 Field observation and additional data sets used

Two campaigns were conducted at an urban site located in the campus of Harbin Institute of Technology (HIT; 45°45'24" N, 126°40'49" E) during the heating seasons of 2018–2019 (from 16 October, 2018 to 14 April, 2019; N = 180) and 2019–2020 (from 16 October, 2019 to 4 February, 2020; N = 112), following the same sampling and analytical procedures. As described for the 2018–2019 campaign (Cheng et al., 2021a), a low volume sampler (MiniVol; Airmetrics, OR, USA) operated at a flow rate of 5 L/min was used to collect airborne PM_{2.5} onto pre-baked quartz-fiber filters (2500 QAT-UP; Pall Corporation, NY, USA), and the measured species included organic carbon (OC), elemental carbon (EC), organic tracers for biomass burning (levoglucosan and mannosan) and water-soluble inorganic ions (sulfate, nitrate, ammonium, etc.). Briefly, OC and EC were determined by a thermal/optical carbon analyzer (DRI-2001; Atmoslytic Inc., CA, USA), using the IMPROVE-A temperature protocol with transmittance charring correction. Precision of the carbon analyzer was investigated by analyzing the samples using another protocol (NIOSH). Comparisons of total carbon and optical attenuation results between the two protocols suggested good repeatability for both the carbon and transmittance measurements (Figure R1). Levoglucosan and mannosan were detected by a Dionex ion chromatography (IC) system (ICS-5000⁺; Thermo Fisher Scientific Inc., MA, USA), using the high-performance anion-exchange chromatography coupled to pulsed amperometric detection (HPAEC-PAD) method. In addition, the IC was also used to measure the inorganic ions. Precision of the IC was evaluated by analyzing selected solutions 5–10 times, and the relative standard deviations were found to be within 5% for all the water-soluble species detected, either organic or inorganic. Based on the observed aerosol components, PM_{2.5} mass was reconstructed as the sum of organic matter (determined as $1.6 \times \text{OC}$), EC and inorganic ions. The reconstructed PM_{2.5} will be specified as (PM_{2.5}) in the flowing discussions.*

Air quality data including PM_{2.5}, sulfur dioxide (SO₂), nitrogen dioxide (NO₂), carbon monoxide (CO), etc. were obtained from China's National Urban Air Quality Real Time Publishing Platform (<http://106.37.208.233:20035/>). They were measured at monitoring sites operated by the China National Environmental Monitoring Center (CNEMC), and could be accessed with a time resolution of 1 hour. There are a total of

12 CNEMC sites in Harbin. Results from the nearest one to the filter sampling site (~2.4 km apart), i.e., Taiping Hongwei Park, were used in this study. In addition, hourly meteorological data including temperature and relative humidity (RH) were obtained from Weather Underground (<https://www.wunderground.com>).

Using levoglucosan as the reference component, the relative abundances of water-soluble potassium (K^+) were found to increase substantially for five samples collected during the Chinese New Year periods in February of 2019 ($N = 2$; Cheng et al., 2021a) and in January of 2020 ($N = 3$; Figure S2), pointing to significant influence of firework emissions. Given that such emissions may result in primary sulfate and nitrate which are difficult to quantify, the firework events were excluded, and the remaining sulfate and nitrate were considered secondary in the following discussions. Then taking together observational results from the filter sampling and CNEMC sites, the sulfur oxidation ratio (SOR) was determined as the molar ratio of sulfate to the sum of sulfate and SO_2 , and the nitrogen oxidation ratio (NOR) was determined similarly based on nitrate and NO_2 .

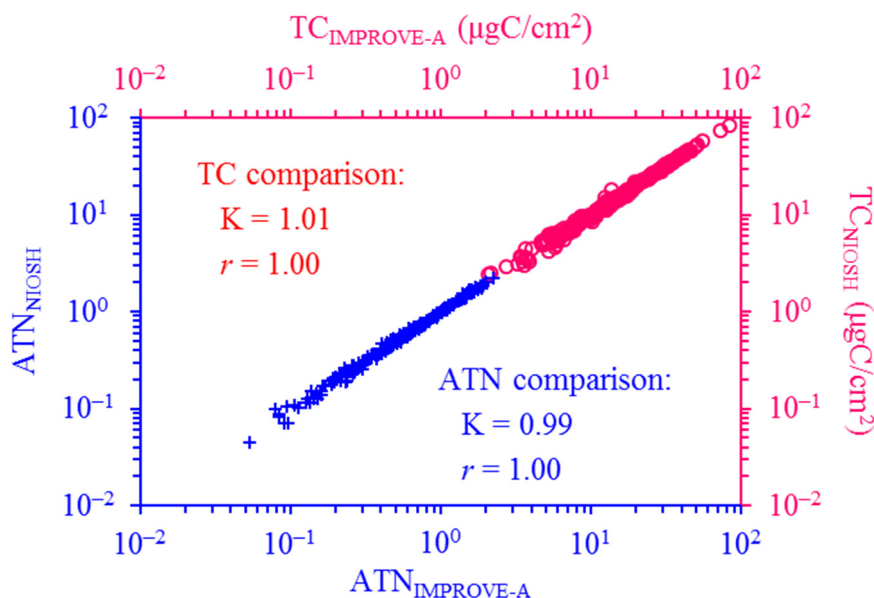


Figure R1. Comparisons of total carbon (TC) and optical attenuation (ATN) measured by different temperature protocols. Results from both campaigns are involved. ATN is calculated as $\ln(I_{final}/I_{initial})$, where $I_{initial}$ and I_{final} indicate filter transmittance signals measured at the beginning (i.e., when the loaded filter has not been heated) and end (i.e., when all the deposited carbon has been combusted off the filter) of thermal-optical analysis, respectively. Linear regression results are shown with K as slope (intercept was set as zero). TC and ATN agreed well between different protocols, demonstrating good precisions for both the carbon and transmittance measurements.

2.2 Thermodynamic simulation

The ISORROPIA-II model (Fountoukis and Nenes, 2007) was used to predict aerosol water content (AWC) and aerosol pH. The calculations were conducted in two ways, namely the “reverse” and “forward” modes. For the “reverse” mode, the measured aerosol-phase data were deployed as input to derive AWC and pH directly. For the “forward” mode, the model was run in an iteration way (Liu et al., 2021a). Briefly, we used the measured aerosol-phase data as initial input, ran ISORROPIA-II in the “forward” mode to predict gas-phase concentrations of semi-volatile species (e.g., ammonia and nitric acid), and used the sum of predicted gas-phase and measured aerosol-phase concentrations as the input for next round. The calculations were repeated until the simulated results were stable and in line with the observational data. Although the “reverse” and “forward” mode simulations showed comparable AWC levels for this campaign (Figure S3), the latter approach has been suggested to give more accurate and robust estimation of pH (Guo et al., 2017; Song et al., 2018). Thus, AWC and pH results predicted by the iteration approach were used in the following discussions.

2.3 Source apportionment

Source apportionment was performed using EPA’s Positive Matrix Factorization (PMF) model (version 5.0), with times series of OC, EC, levoglucosan, chloride, nitrate, sulfate and ammonium from both campaigns as inputs. A total of five factors were resolved, and their profiles were shown in Figure S4. Two factors (BB-1 and BB-2) were strongly associated with primary biomass burning emissions, since almost all the levoglucosan (~90%) were apportioned to these two factors whereas neither of them was a major contributor to secondary ions. Another two factors were inferred to represent secondary aerosols (SA-1 and SA-2), as they had zero EC but the majority of nitrate and sulfate. The last factor (non-BB_{pri}) was attributed to primary emissions from non-BB sources, because more than 50% of EC but little levoglucosan was found in this factor.

The second point raised in this major comment was about the reliability of the PMF analysis. As pointed out by the reviewer, a large number of samples are usually required to get reliable source apportionment results, while the User Guide of PMF recommends that a minimum of 100 samples should be involved in the analysis. In this study, a total of 292 samples were collected, with 180 and 112 from the 2018-2019 and

2019-2020 campaigns, respectively. After excluding those heavily impacted by firework emissions ($N = 5$), all the remaining samples ($N = 287$) were used for the PMF analysis. We think this number of samples could generally be considered acceptable. In addition, we compared the source profiles derived by this study with those obtained by Cheng et al. (2021a), which were based only on the 2018-2019 campaign. As shown by Figure R2, the profiles were quite similar between the two studies. We think this consistency could to some extent support the reliability of the PMF results.

The discussions above were reflected in the revised manuscript (see lines 107-194, 237-246, 318-319, Figures S1 and S4).

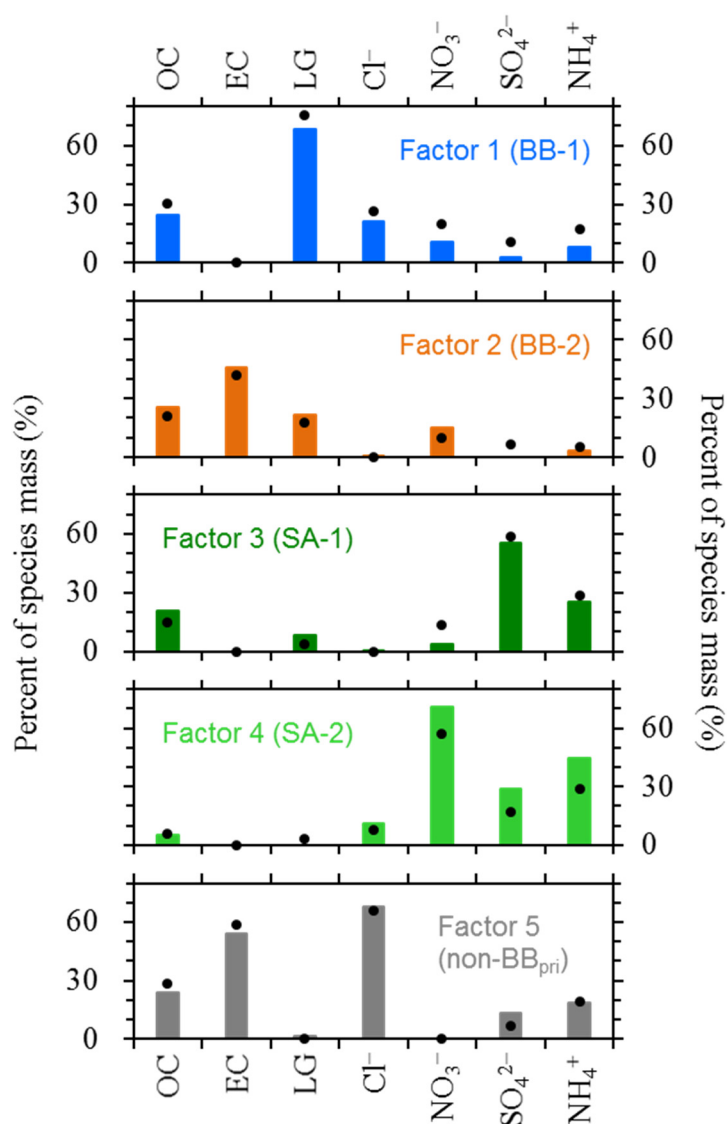


Figure R2. Source profiles resolved by PMF. The solid bars and circles indicate results obtained by this study and Cheng et al. (2021a), respectively. For this study, aerosol compositions measured during the 2018–2019 and 2019–2020 campaigns were

combined and used as the PMF inputs, whereas Cheng et al. (2021a) was based only on the former campaign. In general, similar profiles were resolved by the two studies, despite the different measurement periods covered.

(2) The discussion part is too descriptive and the majority of the main text is just describing the variation of different aerosol components. In some places, the authors jumped to some conclusions without careful investigation. For instance, the RH-dependent increase of OC was attributed to heterogeneous reactions without investigating the cloud-water chemistry and diffusion/dispersion analysis (Line 236-238). Additionally, the author concluded that the inter-annual (I would not call it inter-annual since it is just a two-year comparison) variation of OC was related to RH levels without other vital information of the regional transport pattern and other meteorological parameters. Besides, the higher threshold RH for the sharp increase of SOR in Harbin is not certainly indicative of the fact that the heterogeneous formation of sulfate was less efficient there. Many previous works have pointed out that the polluted air mass from the southern area of Beijing also brings about humidity, rather than heterogeneous chemical reactions at a local/city scale. Thus, some in-depth analysis and rigorous arguments need to be added to this work.

Our responses: We agree with the referee that some discussions in the original manuscript were not sound enough, especially regarding the RH-dependent increase of secondary OC (OC_{sec}), the inter-campaign variation of OC_{sec} , and Harbin's higher threshold RH for sharp increase of SOR compared to Beijing. As pointed by the reviewer, a major problem was that all the observed phenomena were attributed to the influence of atmospheric chemistry, i.e., the roles of other factors such as meteorology and transport were ignored.

In general, air quality modeling is usually required to quantitatively evaluate the contributions of various factors to the variations of $PM_{2.5}$ concentration and composition. If applied to this study, simulations need to be performed for six scenarios: (A–B) actual emissions and meteorological conditions of the 2018–2019 and 2019–2020 measurement periods, respectively; (C) 2018–2019 emissions with 2019–2020 meteorological conditions; (D) 2019–2020 emissions with 2018–2019 meteorological conditions; (E–F) zero emissions from Harbin for the two periods, respectively. The A vs. C and B vs. D differences indicate the influence of meteorology; the A vs. D and B vs. C differences can be attributed to the influence of emissions; the A vs. E and B vs. F differences point to the influence of regional transport. Of course, a precondition for

these simulations is that the model could properly reproduce the observational results. Actually, we have performed the simulation for the 2018–2019 measurement period (i.e., scenario A), using a revised CMAQ model (Hu J. et al., 2016). Compared to the original version (5.0.1), the revised model involved a modified Statewide Air Pollution Research Center (version 11; SAPRC-11) photochemical mechanism, which includes the isoprene epoxydiols (IEPOX) and methacrylic acid epoxide formation pathways, and allows predictions of glyoxal and methylglyoxal formed by oxidation of various precursors including isoprene. In addition, heterogeneous pathways were incorporated into the revised CMAQ to account for secondary inorganic and organic aerosols formed through reactive uptake of gaseous species on aerosol surfaces. The simulations were performed over East Asia with a horizontal resolution of 36×36 km. The meteorological inputs were retrieved from the Weather Research and Forecasting (WRF) model. The emission inputs were generated by combining various inventories, e.g., the Multi-resolution Emission Inventory for China (MEIC; <http://www.meicmodel.org/>) was used to derive anthropogenic emissions of OC, EC, volatile organic compounds (VOCs), SO₂, NO₂, etc., whereas the satellite-based Fire INventory from NCAR (FINN; Wiedinmyer et al., 2011) was used for open burning emissions. When comparing the observational and modeling results, large gaps were observed for two cases. The first one was agricultural fire episodes. For example, the simulated PM_{2.5} accounted for only ~30% of the observed concentrations during February 25 to March 2, 2019, when intensive fire counts were detected (Figure R3a). In addition, the large differences in PM_{2.5} could be attributed mainly to the underestimation of organic aerosol (OA, determined as $1.6\times\text{OC}$) mass by the model, and eventually pointed to the underestimation of open burning emissions by the FINN inventory. The second case was high RH conditions, when enhanced formation of secondary aerosols was evident. Such a period occurred during 12 to 15 January, 2019, showing increased RH (exceeding 80%) and elevated levels of SOR and NOR. The simulated sulfate were substantially lower than the observed concentrations during this period (with averages of ~8 and 27 $\mu\text{g}/\text{m}^3$; Figure R3b), although the model involved both in-cloud and heterogeneous pathways for sulfate formation. The agricultural fire-related underestimation of OA could be resolved by adjusting the open burning emission (Uranishi et al., 2019); however, the RH-related underestimation of sulfate by the revised CMAQ has not been addressed. Thus, we prefer not to conduct additional simulations (e.g., for scenarios B–E) at the current stage.

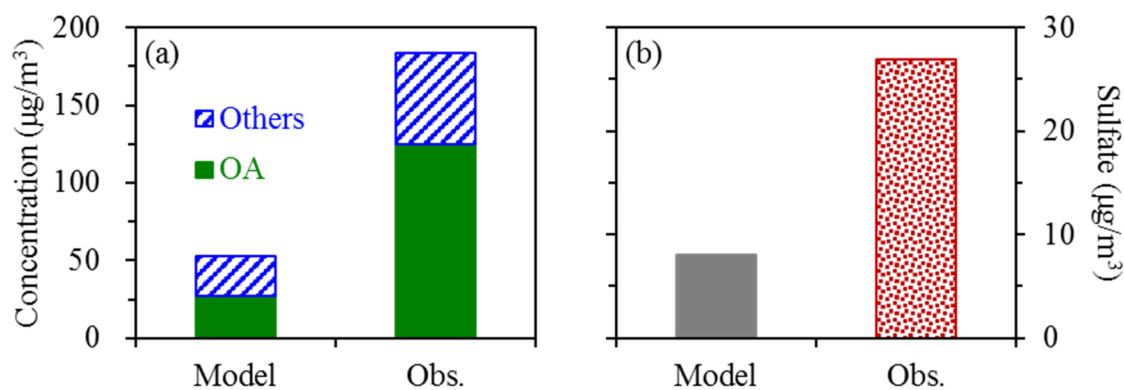


Figure R3. (a) Comparison of modeled and observed $\text{PM}_{2.5}$ for a typical agricultural fire episode, with concentrations of OA and other species shown separately. **(b)** Comparison of modeled and observed sulfate concentrations for a high RH period.

Given that variation of meteorological conditions could indeed influence the absolute concentrations of a given species (e.g., OC_{sec}) but will not change its relative abundances (e.g., the OC_{sec} to OC ratio and the OC_{sec} to EC ratio), in the revised manuscript, the comparisons among different cases (e.g., low-, medium- and high-RH conditions of 2019–2020) were primarily performed using various ratios and fractions. In addition, it was also clearly stated that our discussions on heterogeneous reactions did not exclude the presence of in-cloud chemistry or indicate secondary aerosol formation on a city scale. Specifically, the following changes were made:

(i) The discussions on the OC_{sec} (the second and third paragraphs of section 3.2 in the original manuscript) were reorganized as (see lines 296–329):

As shown in Figure 3, OC_{sec} exhibited a positive dependence on RH, with an explosive increase of OC_{sec} after RH exceeded 80%. Only ~6% of the 2018–2019 samples (10 out of 180) experienced such humid conditions, whereas this fraction was as high as ~37% for 2019–2020 (corresponding to 42 out of the 112 samples). Thus the potential influence of RH on SOA formation was primarily investigated based on results from the 2019–2020 campaign. Figure 4 compares OC source apportionment results across different RH ranges (< 60%, 60–80% and > 80%), which are termed low-, medium- and high-RH conditions, respectively, for this measurement period. Not only OC_{sec} but also its contribution to OC (f_{sec}) increased significantly from the low- through high-RH conditions, by factors of 9.8 and 2.6, respectively. Although the 2019–2020 campaign experienced much lower ambient temperatures (as low as $-20\text{ }^{\circ}\text{C}$) compared to Beijing’s winter ($\sim 0\text{ }^{\circ}\text{C}$), the f_{sec} of Harbin reached 42% for the RH range of > 80%, generally comparable with the typical range of oxygenated organic aerosol (OOA)

contribution (~35–60%) determined under humid winter conditions in Beijing (Sun et al., 2013, 2014, 2018; Hu et al., 2016; Xu et al., 2019). Given the considerable AWC levels predicted for the high-RH conditions (typically above 50 $\mu\text{g}/\text{m}^3$; Figure 3), it was inferred that heterogeneous reactions might be at play in the RH-dependent increase of f_{sec} .

(ii) The statement arguing the less efficient sulfate formation in Harbin was removed (see lines 372-373):

However, the threshold RH for sharp increase of SOR was higher in Harbin (80%) than that in Beijing (~40–70%), and the SOR in Harbin with RH above 80% (averaging 0.2) were at the lower end of those the corresponding values observed during winter in Beijing (typically with averages of ~0.2–0.6) (Sun et al., 2013; Zheng et al., 2015b; Zhang et al., 2018; Li et al., 2019; Liu et al., 2020). A likely cause for these differences was the relatively low temperatures during the measurement period, which would reduce the rate coefficients of relevant aqueous-phase reactions (Cheng et al., 2016).

(iii) Conclusions and implications were presented in separate sections, with the limitations of this study (i.e., the future work that needs to be done) being clearly stated (see lines 469, 495 and 514-523):

It should be noted that the discussions on heterogeneous formation of SOA and SNA did not necessarily exclude the reactions in fog/cloud water. Actually, based on the observational results available, we could not robustly distinguish the relative importance of various aqueous-phases pathways for secondary aerosol formation. To address this problem, air quality modeling with a focus on HC should be conducted in future studies, which could also quantitatively evaluate the contributions of various factors (e.g., meteorology, emissions and regional transport) to long-term trends of $\text{PM}_{2.5}$ concentration and chemical composition. An essential precondition is that the model could properly re-produce the observational results, which appears a substantial challenge for Harbin as indicated by the limited inter-comparison studies, especially for the periods with intensive agricultural fires or high RH levels (Cheng et al., 2021b).

(3) There are also some inconsistent arguments that needed to be checked. For instance, in the abstract, the authors claimed that "we found that open burning activities were actually not eliminated", but Line 168 stated that "indicating that agricultural fires

were almost completely eliminated during the measurement period". It doesn't seem very clear.

Our responses: Regarding the open burning activities under the “strict prohibition” policy, the message we would like to convey was actually that “although not occurred during the 2019–2020 measurement period, agricultural fires broke out within a short period before crop planting in spring of 2020”. All the inconsistent/misleading descriptions were corrected in the revised manuscript. In addition, the use of “inter-annual” was avoided following the suggestion raised in the major comment #2. (See lines 36, 234, 315 and 472).

References

- Cheng, Y., Yu, Q. Q., Liu, J. M., Du, Z. Y., Liang, L. L., Geng, G. N., Zheng, B., Ma, W. L., Qi, H., Zhang, Q., and He, K.B.: Strong biomass burning contribution to ambient aerosol during heating season in a megacity in Northeast China: effectiveness of agricultural fire bans?, *Sci. Total Environ.*, 754, 142144, 2021a.
- Cheng, Y., Yu, Q. Q., Liu, J. M., Zhu, S. Q., Zhang, M. Y., Zhang, H. L., Zheng, B., and He, K. B.: Model vs. observation discrepancy in aerosol characteristics during a half-year long campaign in Northeast China: the role of biomass burning, *Environ. Pollut.*, 269, 116167, 2021b.
- Cheng, Y. F., Zheng, G. J., Wei, C., Mu, Q., Zheng, B., Wang, Z. B., Gao, M., Zhang, Q., He, K. B., Carmichael, G., Pöschl, U., and Su, H.: Reactive nitrogen chemistry in aerosol water as a source of sulfate during haze events in China, *Sci. Adv.*, 2, e1601530, 2016.
- Fountoukis, C., and Nenes, A.: ISORROPIA II: a computationally efficient thermodynamic equilibrium model for $K^+Ca^{2+}Mg^{2+}NH_4^+Na^+SO_4^{2-}NO_3^-Cl^-H_2O$ aerosols, *Atmos. Chem. Phys.*, 7, 4639–4659, 2007.
- Guo, H. Y., Liu, J. M., Froyd, K. D., Roberts, J. M., Veres, P. R., Hayes, P. L., Jimenez, J. L., Nenes, A., and Weber, R. J.: Fine particle pH and gas–particle phase partitioning of inorganic species in Pasadena, California, during the 2010 CalNex campaign, *Atmos. Chem. Phys.*, 17, 5703–5719, 2017.
- Hu, J. L., Chen, J. J., Ying, Q., and Zhang, H. L.: One-year simulation of ozone and particulate matter in China using WRF/CMAQ modeling system, *Atmos. Chem. Phys.*, 16, 10333–10350, 2016.
- Hu, W. W., Hu, M., Hu, W., Jimenez, J. L., Yuan, B., Chen, W. T., Wang, M., Wu, Y. S., Chen, C., Wang, Z. B., Peng, J. F., Zeng, L. M., and Shao, M.: Chemical composition, sources, and aging process of submicron aerosols in Beijing: contrast between summer and winter, *J. Geophys. Res. Atmos.*, 121, 1955–1977, 2016.

- Li, H. Y., Cheng, J., Zhang, Q., Zheng, B., Zhang, Y. X., Zheng, G. J., and He, K. B.: Rapid transition in winter aerosol composition in Beijing from 2014 to 2017: response to clean air actions, *Atmos. Chem. Phys.*, 19, 11485–11499, 2019.
- Liu, P. F., Ye, C., Xue, C. Y., Zhang, C. L., Mu, Y. J., and Sun, X.: Formation mechanisms of atmospheric nitrate and sulfate during the winter haze pollution periods in Beijing: gas-phase, heterogeneous and aqueous-phase chemistry, *Atmos. Chem. Phys.*, 20, 4153–4165, 2020.
- Song, S. J., Gao, M., Xu, W. Q., Shao, J. Y., Shi, G. L., Wang, S. X., Wang, Y. X., Sun, Y. L., and McElroy, M. B.: Fine-particle pH for Beijing winter haze as inferred from different thermodynamic equilibrium models, *Atmos. Chem. Phys.*, 18, 7423–7438, 2018.
- Sun, Y. L., Jiang, Q., Wang, Z. F., Fu, P. Q., Li, J., Yang, T., and Yin, Y.: Investigation of the sources and evolution processes of severe haze pollution in Beijing in January 2013, *J. Geophys. Res. Atmos.*, 119, 4380–4398, 2014.
- Sun, Y. L., Wang, Z. F., Fu, P. Q., Jiang, Q., Yang, T., Li, J., and Ge, X. L.: The impact of relative humidity on aerosol composition and evolution processes during wintertime in Beijing, China, *Atmos. Environ.*, 77, 927–934, 2013.
- Sun, Y. L., Xu, W. Q., Zhang, Q., Jiang, Q., Canonaco, F., Prévôt, A. S. H., Fu, P. Q., Li, J., Jayne, J., Worsnop, D. R., and Wang, Z. F.: Source apportionment of organic aerosol from 2-year highly time-resolved measurements by an aerosol chemical speciation monitor in Beijing, China, *Atmos. Chem. Phys.*, 18, 8469–8489, 2018.
- Wiedinmyer, C., Akagi, S. K., Yokelson, R. J., Emmons, L. K., Al-Saadi, J. A., Orlando, J. J., and Soja, A. J.: The Fire INventory from NCAR (FINN): a high resolution global model to estimate the emissions from open burning, *Geosci. Model Dev.*, 4, 625–641, 2011.
- Xu, W. Q., Sun, Y. L., Wang, Q. Q., Zhao, J., Wang, J. F., Ge, X. L., Xie, C. H., Zhou, W., Du, W., Li, J., Fu, P. Q., Wang, Z. F., Worsnop, D. R., and Coe, H.: Changes in aerosol chemistry from 2014 to 2016 in winter in Beijing: insights from high-resolution aerosol mass spectrometry, *J. Geophys. Res. Atmos.*, 124, 1132–1147, 2019.
- Zhang, R., Sun, X. S., Shi, A. J., Huang, Y. H., Yan, J., Nie, T., Yan, X., Li, X.: Secondary inorganic aerosols formation during haze episodes at an urban site in Beijing, China, *Atmos. Environ.*, 177, 275–282, 2018.
- Zheng, G. J., Duan, F. K., Su, H., Ma, Y. L., Cheng, Y., Zheng, B., Zhang, Q., Huang, T., Kimoto, T., Chang, D., Pöschl, U., Cheng, Y. F., and He, K. B.: Exploring the severe winter haze in Beijing: the impact of synoptic weather, regional transport and heterogeneous reactions, *Atmos. Chem. Phys.*, 15, 2969–2983, 2015.

Dramatic changes in Harbin aerosol during 2018–2020: the roles of open burning policy and secondary aerosol formation

Yuan Cheng¹, Qin-qin Yu¹, Jiu-meng Liu^{1,*}, Xu-bing Cao¹, Ying-jie Zhong¹, Zhen-yu Du², Lin-lin Liang³, Guan-nan Geng⁴, Wan-li Ma¹, Hong Qi¹, Qiang Zhang⁵, Ke-bin He⁴

¹ State Key Laboratory of Urban Water Resource and Environment, School of Environment, Harbin Institute of Technology, Harbin, China

² National Research Center for Environmental Analysis and Measurement, Environmental Development Center of the Ministry of Ecology and Environment, Beijing, China

³ State Key Laboratory of Severe Weather & CMA Key Laboratory of Atmospheric Chemistry, Chinese Academy of Meteorological Sciences, Beijing, China

⁴ State Key Joint Laboratory of Environment Simulation and Pollution Control, School of Environment, Tsinghua University, Beijing, China

⁵ Department of Earth System Science, Tsinghua University, Beijing, China

* Corresponding author. Jiu-meng Liu (jiumengliu@hit.edu.cn).

Abstract

Despite the growing interest in understanding haze formation in Chinese megacities, air pollution has been largely overlooked for the Harbin-Changchun (HC) metropolitan area located in the severe cold climate region in Northeast China. In this study, we unfolded significant variations of fine particulate matter (PM_{2.5}) in HC's central city (Harbin) during two sequential heating seasons of 2018–2019 and 2019–2020, and explored major drivers for the observed variations. The two campaigns showed comparable organic carbon (OC) levels but quite different OC sources. The biomass burning (BB) to OC contribution decreased substantially for 2019–2020, which was attributed primarily to the transition of local policies on agricultural fires, i.e., from the “legitimate burning” policy released in 2018 to the “strict prohibition” policy in 2019. Meanwhile, the contribution of secondary OC (OC_{sec}) increased significantly, associated with the much more frequent occurrences of high relative humidity (RH) conditions during the 2019–2020 measurement

period. Similar to OC_{sec} , the major secondary inorganic ions, i.e., sulfate, nitrate and ammonium (SNA), also exhibited RH-dependent increases. Given the considerable aerosol water contents predicted for the high-RH conditions, heterogeneous reactions were likely at play in secondary aerosol formation even in the frigid atmosphere in Harbin (e.g., with daily average temperatures down to below $-20\text{ }^{\circ}\text{C}$). In brief, compared to 2018–2019, the 2019–2020 measurement period was characterized by a policy-driven decrease of biomass burning OC, a RH-related increase of OC_{sec} and a RH-related increase of SNA, with the former two factors generally offsetting each other. In addition, we found that open burning activities were actually not eliminated by the “strict prohibition” policy released in 2019, based on a synthesis of air quality data and fire count results. Although not ~~evident throughout~~ occurred during the 2019–2020 measurement period, agricultural fires broke out within a short period before crop planting in spring of 2020, and resulted in off-the-chart air pollution for Harbin, with 1- and 24-hour $PM_{2.5}$ concentrations peaking at ~ 2350 and $900\text{ }\mu\text{g}/\text{m}^3$, respectively. This study indicates that sustainable use of crop residues remains a difficult challenge for the massive agricultural sector in Northeast China.

1. Introduction

Despite nationwide reductions in anthropogenic emissions (Zhang et al., 2019), severe haze pollution characterized by high concentrations of fine particulate matter (PM_{2.5}) is far from being effectively controlled in China, e.g., haze episodes were observed in Beijing even during the COVID-19 lockdown (Lv et al., 2020). This reveals the complex yet poorly understood responses of air pollution to changes of primary emission. While secondary aerosol production has been thought to be largely responsible for this lack of understanding, the chemical mechanisms remain vague (Le et al., 2020; Wang et al., 2020b; Huang et al., 2021). For example, state-of-the-art models incorporating gas-phase and cloud chemistry frequently underestimated sulfate and secondary organic aerosol (SOA) concentrations for winter haze events in Beijing (Wang et al., 2014; Zheng et al., 2015a; Cheng et al., 2016; Liu et al., 2020a). The underestimation was more significant with increasing relative humidity (RH) or aerosol water content (AWC) levels, pointing to the importance of aqueous-phase reactions in aerosol water (Wang et al., 2016; Shrivastava et al., 2017; Su et al., 2020; Liu et al., 2021b). On the other hand, quantitative prediction of secondary ~~aerosol~~ aerosols formed through aqueous-phase reactions remains challenging, partially due to uncertainties in aerosol pH (Guo et al., 2017b; Song et al., 2018; Zheng et al., 2020) and oxidant concentrations (Ye et al., 2018; Wang et al., 2020a). In addition, despite the role of heterogeneous chemistry has been widely accepted for sulfate formation, ~~the~~ its effects on SOA remain unclear, with more evidences indicating an enhancement effect (Hu et al., 2016; Kuang et al., 2020; Liu et al., 2020a; Wang et al., 2021a) overwhelming those suggesting little influence of RH or AWC on SOA formation (Zheng et al., 2015b). In all, there is a growing interest in understanding haze pollution in Chinese megacities (Shi et al., 2019), especially regarding the driving factors responsible for the spatio-temporal

variations, since these factors are essential for the development of efficient air pollution control strategies.

Studies on haze in China have been historically concentrated in the North China Plain (NCP), especially around Beijing. Recently, new hotspots began to emerge, e.g., the Harbin-Changchun (HC) metropolitan area. HC is located in the severe cold climate region in Northeast China, and includes 11 cities in the two provinces of Heilongjiang and Jilin. Compared to NCP and other traditional hotspots of air pollution research (e.g., the Yangtze River Delta), HC is characterized by its extremely cold winter when the daily average temperatures could drop to below -20°C . Thus, the heating season is usually as long as six months in HC, lasting from late fall through early spring of next year. During this period, intensive energy use is expected, e.g., coal combustion for central heating in urban areas and household biomass burning for space-heating in rural areas. The intensive energy use, to a large extent, determines the relatively high baseline of $\text{PM}_{2.5}$ pollution in HC's heating season. According to the open access air quality data routinely published by China National Environmental Monitoring Center (<http://106.37.208.233:20035/>), the monthly averages of $\text{PM}_{2.5}$ measured during winter in Harbin stayed above $55\text{ }\mu\text{g}/\text{m}^3$ from 2013 throughout 2020, whereas the corresponding value could drop to below $30\text{ }\mu\text{g}/\text{m}^3$ for Beijing.

Another feature of HC is that it is located in a main agricultural region in China. For example, Heilongjiang Province provided $\sim 13\%$ and 15% of the national rice and corn productions in 2019, respectively, with only $\sim 5\%$ of China's land area (National Bureau of Statistics of China, 2020). The massive agricultural sector results in a huge amount of crop residues, which are produced after harvesting in autumn and must be disposed before planting in spring of the next year. Although nominally prohibited, open burning persists as an important approach for the disposal of crop

residues in Northeast China, with a time window largely overlapped with the heating season. These agricultural fires frequently resulted in heavily-polluted PM_{2.5} episodes, e.g., with 24-hour PM_{2.5} peaking at ~650 µg/m³ during early November of 2015 in Harbin (Li et al., 2019b). Given that the agricultural fires were never eliminated, interim provisions were released by Heilongjiang Province in 2018, which approved a window of approximately 3 months (from 11 December, 2018 to 9 March, 2019) for open burning of crop residues (Department of Ecology and Environment of Heilongjiang Province, 2018). However, the interim provisions were amended in 2019, i.e., the “legitimate burning” policy was terminated and was replaced by a toughest-ever policy on open burning, which required that agricultural fires should be strictly prohibited for the period of 15 September, 2019 to 15 May, 2020. The rapid transition of open burning policy reflects the ongoing attempts of local government to control the severe haze pollution caused by agricultural fires. However, the most effective and reliable approach remains inconclusive, given that very little is known about the role of biomass burning in PM_{2.5} pollution in Northeast China. Actually, PM_{2.5} in Northeast China is far from being well characterized yet with ~~the~~ limited studies (e.g., Cao et al., 2016; Yang et al., 2017; Li et al., 2019b; Zhang et al., 2020), especially regarding sources and chemical mechanisms of aerosol formation.

In this study, we investigated the variations of Harbin aerosol during two sequential heating seasons of 2018–2019 and 2019–2020, with focuses on the roles of (1) rapid transition of open burning policy and (2) significant change of meteorological conditions (especially relative humidity), which would influence primary emissions and secondary aerosol formation, respectively. Policy implications for improving air quality in the HC region were also discussed.

2. Methods

2.1 Field observation and additional data sets used

Two campaigns were conducted at an urban site located in the campus of Harbin Institute of Technology (HIT; 45°45'24" N, 126°40'49" E) during the heating seasons of 2018–2019 (from 16 October, 2018 to 14 April, 2019; $N = 180$) and 2019–2020 (from 16 October, 2019 to 4 February, 2020; $N = 112$), following the same sampling and analytical procedures. As described for the 2018–2019 campaign (Cheng et al., 2021a), a low volume sampler (MiniVol; Airmetrics, OR, USA) operated at a flow rate of 5 L/min was used to collect airborne $PM_{2.5}$ onto pre-baked quartz-fiber filters (2500 QAT-UP; Pall Corporation, NY, USA), and the measured species included organic carbon (OC), elemental carbon (EC), organic tracers for biomass burning (levoglucosan and mannosan) and water-soluble inorganic ions (sulfate, nitrate, ammonium, etc.). Briefly, OC and EC were determined by a thermal/optical carbon analyzer (DRI-2001; Atmoslytic Inc., CA, USA), using the IMPROVE-A temperature protocol with transmittance charring correction. Precision of the carbon analyzer was investigated by analyzing the samples using another protocol (NIOSH). Comparisons of total carbon and optical attenuation results between the two protocols suggested good repeatability for both the carbon and transmittance measurements (Figure S1). Levoglucosan and mannosan were detected by a Dionex ion chromatography (IC) system (ICS-5000⁺; Thermo Fisher Scientific Inc., MA, USA), using the high-performance anion-exchange chromatography coupled to pulsed amperometric detection (HPAEC-PAD) method. In addition, the IC was also used to measure the inorganic ions. Precision of the IC was evaluated by analyzing selected solutions 5–10 times, and the relative standard deviations were found to be within 5% for all the water-soluble species detected, either organic or inorganic. Based on the observed aerosol components, $PM_{2.5}$ mass was reconstructed as the sum of organic matter (determined as $1.6 \times OC$), EC and inorganic ions.

The reconstructed $\text{PM}_{2.5}$ will be specified as $(\text{PM}_{2.5})^*$ in the following discussions.

Air quality data including $\text{PM}_{2.5}$, sulfur dioxide (SO_2), nitrogen dioxide (NO_2), carbon monoxide (CO), etc. were obtained from China's National Urban Air Quality Real Time Publishing Platform (<http://106.37.208.233:20035/>). They were measured at monitoring sites operated by the China National Environmental Monitoring Center (CNEMC), and could be accessed with a time resolution of 1 hour. There are a total of 12 CNEMC sites in Harbin. Results from the nearest one to the filter sampling site (~2.4 km apart), i.e., Taiping Hongwei Park, were used in this study. In addition, hourly meteorological data including temperature and relative humidity (RH) were obtained from Weather Underground (<https://www.wunderground.com>).

Using levoglucosan as the reference component, the relative abundances of water-soluble potassium (K^+) were found to increase substantially for five samples collected during the Chinese New Year periods in February of 2019 ($N = 2$; Cheng et al., 2021a) and in January of 2020 ($N = 3$; Figure S2), pointing to significant influence of firework emissions. Given that such emissions may result in primary sulfate and nitrate which are difficult to quantify, the firework events were excluded, and the remaining sulfate and nitrate were considered secondary in the following discussions. Then taking together observational results from the filter sampling and CNEMC sites, the sulfur oxidation ratio (SOR) was determined as the molar ratio of sulfate to the sum of sulfate and SO_2 , and the nitrogen oxidation ratio (NOR) was determined similarly based on nitrate and NO_2 .

2.2 Thermodynamic simulation

The ISORROPIA-II model (Fountoukis and Nenes, 2007) was used to predict aerosol water content (AWC) and aerosol pH. The calculations were conducted in two ways, namely the “reverse” and “forward” modes. For the “reverse” mode, the measured aerosol-phase data were deployed as

input to derive AWC and pH directly. For the “forward” mode, the model was run in an iteration way (Liu et al., 2021a). Briefly, we used the measured aerosol-phase data as initial input, ran ISORROPIA-II in the “forward” mode to predict gas-phase concentrations of semi-volatile species (e.g., ammonia and nitric acid), and used the sum of predicted gas-phase and measured aerosol-phase concentrations as the input for next round. The calculations were repeated until the simulated results were stable and in line with the observational data. Although the “reverse” and “forward” mode simulations showed comparable AWC levels for this campaign (Figure S3), the latter approach has been suggested to give more accurate and robust estimation of pH (Guo et al., 2017a; Song et al., 2018). Thus, AWC and pH results predicted by the iteration approach were used in the following discussions.

2.3 Source apportionment

Source apportionment was performed using EPA’s Positive Matrix Factorization (PMF) model (version 5.0), with times series of OC, EC, levoglucosan, chloride, nitrate, sulfate and ammonium from both campaigns as inputs. A total of five factors were resolved, and their profiles were shown in Figure S4. Two factors (BB-1 and BB-2) were strongly associated with primary biomass burning emissions, since almost all the levoglucosan (~90%) were apportioned to these two factors whereas neither of them was a major contributor to secondary ions. Another two factors were inferred to represent secondary aerosols (SA-1 and SA-2), as they had zero EC but the majority of nitrate and sulfate. The last factor (non-BB_{pri}) was attributed to primary emissions from non-BB sources, because more than 50% of EC but little levoglucosan was found in this factor.

~~Two campaigns were conducted at an urban site located in the campus of Harbin Institute of Technology (HIT) during the heating seasons of 2018–2019 (from 16 October, 2018 to 14 April,~~

2019; $N=180$) and 2019–2020 (from 16 October, 2019 to 4 February, 2020; $N=112$), following the same sampling and analytical procedures. As described for the 2018–2019 campaign (Cheng et al., 2021), a low-volume sampler operated at a flow rate of 5 L/min was used to collect airborne $\text{PM}_{2.5}$ onto pre-baked quartz-fiber filters, and the chemical components quantified included organic carbon (OC), elemental carbon (EC), organic tracers for biomass burning (levoglucosan and mannosan) and water-soluble inorganic ions (sulfate, nitrate, ammonium, etc.). Based on the measured species, $\text{PM}_{2.5}$ mass was reconstructed as the sum of organic matter (determined as $1.6 \times \text{OC}$), EC and inorganic ions. The reconstructed $\text{PM}_{2.5}$ will be specified as $(\text{PM}_{2.5})^{\text{R}}$ in the following discussions. In addition to the observational results from HIT, online data sets were used to obtain hourly meteorological data such as temperature and relative humidity (RH), and air quality data including $\text{PM}_{2.5}$, inhalable particles (PM_{10}), sulfur dioxide (SO_2), nitrogen dioxide (NO_2), carbon monoxide (CO) and ozone (O_3). Refer to supplementary material for details on the field measurement and collection of additional data.

Using levoglucosan as the reference component, the relative abundances of water-soluble potassium (K^+) were found to increase substantially for five samples collected during the Chinese New Year periods in February of 2019 ($N=2$; Cheng et al., 2021) and in January of 2020 ($N=3$; Figure S1), pointing to significant influence of firework emissions. Given that such emissions may result in primary sulfate and nitrate which are difficult to quantify, the firework events were excluded, and the remaining sulfate and nitrate were considered secondary in the following discussions. Correspondingly, the sulfur oxidation ratio (SOR) was determined as the molar ratio of sulfate to the sum of sulfate and SO_2 , and the nitrogen oxidation ratio (NOR) was determined similarly based on nitrate and NO_2 .

3. Results and discussion

3.1 Variation of biomass burning (BB) OC

Although comparable OC levels were observed during the 2018–2019 and 2019–2020 measurement periods (averaging 20.66 ± 18.17 and $20.64 \pm 16.76 \mu\text{gC}/\text{m}^3$, respectively), the former campaign exhibited substantially higher contributions of levoglucosan to OC (Figure 1a). Here we applied the levoglucosan to OC ratio (LG/OC) as the indicator for BB impact, given that the absolute concentrations of ambient levoglucosan could be influenced by other factors in addition to biomass burning (e.g., wind speed and planetary boundary layer height). LG/OC averaged 1.83 ± 1.18 and $1.17 \pm 0.30\%$ (on a basis of carbon mass) during 2018–2019 and 2019–2020, respectively, indicating that the influence of biomass burning was stronger during the former campaign. This difference was mainly caused by the 2018–2019 samples collected during and after the “legitimate burning” periods (periods of P-2 and P-3, with average LG/OC ratios of 2.09 ± 1.42 and $2.15 \pm 0.94\%$, respectively; Figure 1b), whereas the LG/OC ratios observed before the onset of “legitimate burning” (P-1, averaging $1.20 \pm 0.36\%$) were in general comparable with those during the 2019–2020 campaign.

Recalling the different open burning policies released in 2018 and 2019, the observed variations of LG/OC appeared to be associated with agricultural fires. According to the relationship between levoglucosan and OC, Cheng et al. (2021a) classified the 2018–2019 samples into three groups (Cases A, B and C) with LG/OC ranges of $< 1.5\%$, $1.5\text{--}3.0\%$ and $> 3.0\%$, respectively. Levoglucosan exhibited strong linear correlations with OC for all the three cases ($r \geq 0.95$), with slopes, i.e., $\Delta\text{LG}/\Delta\text{OC}$ (approximately equivalent to LG/OC given the close-to-zero intercepts), of 1.1, 2.3 and 5.0%, respectively. The variation of LG/OC across the three cases was inferred to be driven mainly by agricultural fires that had relatively low combustion efficiencies, based on a

synthesis of the following evidences (Cheng et al., 2021a): (1) the levoglucosan to K^+ ratios and levoglucosan to mannosan ratios observed throughout the 2018–2019 campaign were in line with the characteristics of BB smoke emitted by the burning of crop residues; (2) no dependence of LG/OC on temperature was observed, indicating that the variations of LG/OC could not be explained by biomass burning for household space-heating in rural areas; (3) elevated LG/OC ratios were typically associated with intensive fire counts, i.e., open burning of crop residues, around Harbin; (4) chemical signatures associated with combustion phase exhibited changes toward smoldering-dominated burning from Cases A through C, e.g., $\Delta EC/\Delta CO$ (derived from linear regression of EC on CO) decreased whereas the levoglucosan to K^+ ratios increased. Following Cheng et al. (2021a), LG/OC ratios higher than 1.5% were considered an indicator for apparent impacts of agricultural fires around Harbin. As shown in Figures 1c–1d, approximately 50% of the 2018–2019 samples exhibited LG/OC above 1.5%, with various fractions for the three periods, i.e., 15, 64 and 71% for P-1, P-2 and P-3 samples, respectively. Thus, apparent impacts of agricultural fires were frequently encountered in the 2018–2019 campaign, particularly after the onset of “legitimate burning”. It is noteworthy that the agricultural fires did not actually disappear after the ending of “legitimate burning” and instead extended to mid-April of 2019. For the 2019–2020 campaign, however, only less than 5% of the samples showed LG/OC larger than 1.5% (Figure 1c), indicating ~~that the rare occurrence of agricultural fires were almost completely eliminated~~ during the measurement period.

Comparison of source apportionment results between the two campaigns also indicated substantial changes in the influence of agricultural fires. ~~In this study, source apportionment was performed using EPA’s Positive Matrix Factorization (PMF) model (version 5.0), with OC, EC,~~

~~levoglucosan, chloride, nitrate, sulfate and ammonium from both campaigns as inputs. A total of~~
~~five factors were resolved, and their profiles were shown in Figure S2. Two factors (BB-1 and BB-~~
~~2) were strongly associated with primary biomass burning emissions, since almost all the~~
~~levoglucosan (~90%) were apportioned to these two factors whereas neither of them was a major~~
~~contributor to secondary ions. Another two factors were inferred to represent secondary aerosols~~
~~(SA-1 and SA-2), as they had little EC but the majority of nitrate and sulfate. The last factor (non-~~
~~BB_{PH}) was attributed to primary emissions from non-BB sources, because more than 50% of EC but~~
~~little levoglucosan was found in this factor.~~ For the 2018–2019 campaign, both the OC mass
 apportioned to BB-1 (OC_{BB-1}; Figure S5) and the contribution of BB-1 to OC (f_{BB-1} ; Figure 2)
 increased substantially after the onset of “legitimate burning”, likely indicating that this factor was
 representative of agricultural fire emissions. This inference was also supported by the comparison
 of OC source apportionment results across the three cases (A–C) with increasing LG/OC ratios, i.e.,
 with stronger impacts of agricultural fires. OC_{BB-1} increased drastically by ~25 folds (from 1.2 to
 30.9 $\mu\text{gC}/\text{m}^3$) from Cases A through C, with OC attributed to other factors being largely unchanged,
 and correspondingly, f_{BB-1} increased sharply from 9 to 69% across the three cases (Figure S6). In
 addition, it was noticed that negligible EC was apportioned to the BB-1 factor (Figure S4), which
 was the characteristic of smoldering-dominated combustion as supported by numerous BB source
 emission studies (McMeeking et al., 2009; May et al., 2014; Pokhrel et al., 2016; McClure et al.,
 2020; Wang et al., 2020c). This feature was consistent with the inference that the agricultural fires
 had relatively low combustion efficiencies (Cheng et al., 2021a). During the 2018–2019 campaign,
 the contribution of agricultural fires to OC was rather small (9%) before the onset of “legitimate
 burning”, whereas after this time point, the contribution increased to ~40% (Figure 2). The overall

f_{BB-1} was 34% for the entire measurement period of 2018–2019, suggesting agricultural fire emissions as the dominant source of OC. For the 2019–2020 campaign, however, f_{BB-1} was substantially lower (9%; Figure 2), comparable with that determined for the 2018–2019 samples collected during P-1, i.e., before the onset of “legitimate burning”. Regarding the temporal variation of agricultural fire impacts, therefore, the same patterns were observed based on the comparisons of LG/OC and PMF results across various measurement periods.

Unlike OC_{BB-1} , OC masses apportioned to the BB-2 factor (OC_{BB-2}) were comparable for the 2018–2019 samples collected before, during and after the “legitimate burning” periods (Figure S5). OC_{BB-2} was also largely unchanged across the three cases (A–C) with stronger impacts of agricultural fires (Figure S6). Therefore, it seems that BB-2 was associated with biomass burning activities that did not have significant daily variation, with the most likely candidate being household combustion of crop residues (for cooking and heating). In addition, OC_{BB-2} appeared to be slightly higher for the 2019–2020 campaign compared to 2018–2019 (6.24 vs. 4.51 $\mu\text{gC}/\text{m}^3$; Figure S5), presumably because more crop residues were consumed through household use ~~during~~ ~~2019–2020~~ in response to the “strict prohibition” open burning policy.

The two biomass burning factors constituted 57% of OC for the 2018–2019 campaign (Figure 2). Before the onset of “legitimate burning”, the total contribution of biomass burning (f_{BB}) was 46% and was dominated by the BB-2 factor (i.e., household burning of crop residues), whereas after this time point, f_{BB} increased to 59% and was dominated by BB-1 (agricultural fires). For the Case C samples, i.e., under the strongest impacts of agricultural fires, f_{BB} was as high as 79% (Figure S6). A prominent reduction in OC_{BB-1} , however, occurred for the 2019–2020 measurement period, and f_{BB} dropped to 39% with BB-2 as the dominant ~~driver~~ contributor (Figures 2 and S5). It is

noteworthy that compared to the typical f_{BB} determined during winter in Beijing (~10–20%, derived from field observations using aerosol mass spectrometer; Hu et al., 2016; Sun et al., 2018; Li et al., 2019a; Xu et al., 2019), the BB contributions were much higher in Harbin even when the contribution of agricultural fires was limited (e.g., during the 2019–2020 campaign, and P-1 in 2018–2019), pointing to strong emissions from residential burning of crop residues throughout the heating season in Northeast China.

3.2 Variation of secondary OC

OC masses apportioned to the SA-1 and SA-2 factors (OC_{sec}) were considered secondary. OC_{sec} were 3.9 and 7.6 $\mu\text{gC}/\text{m}^3$ for the 2018–2019 and 2019–2020 campaigns, respectively, constituting 19 and 37% of OC (Figures 2 and S5). It was noticed that for biomass burning OC and OC_{sec} , their inter-campaign differences showed comparable absolute values but opposite signs. This explains why the two heating seasons had significantly different OC sources but almost the same OC levels ~~average concentrations~~.

As shown in Figure 3, OC_{sec} exhibited a positive dependence on RH, with an explosive increase of OC_{sec} after RH exceeded 80%. Only ~6% of the 2018–2019 samples (10 out of 180) experienced such humid conditions, whereas this fraction was as high as ~37% for 2019–2020 (corresponding to 42 out of the 112 samples). Thus the potential influence of RH on SOA formation was primarily investigated based on results from the 2019–2020 campaign. Figure 4 compares OC source apportionment results across different RH ranges (< 60%, 60–80% and > 80%), which are termed low-, medium- and high-RH conditions, respectively, for this measurement period. Not only OC_{sec} but also its contribution to OC (f_{sec}) increased significantly from the low- through high-RH conditions, by factors of 9.8 and 2.6, respectively. Although the 2019–2020 campaign experienced

much lower ambient temperatures (as low as $-20\text{ }^{\circ}\text{C}$) compared to Beijing's winter ($\sim 0\text{ }^{\circ}\text{C}$), the f_{sec} of Harbin reached 42% for the RH range of $> 80\%$, generally comparable with the typical range of oxygenated organic aerosol (OOA) contribution ($\sim 35\text{--}60\%$) determined under humid winter conditions in Beijing (Sun et al., 2013, 2014, 2018; Hu et al., 2016; Xu et al., 2019). Given the considerable AWC levels predicted for the high-RH conditions (typically above $50\text{ }\mu\text{g}/\text{m}^3$; Figure 3), it was inferred that heterogeneous reactions might be at play in the RH-dependent increase of f_{sec} .

~~As shown in Figure 3, OC_{sec} exhibited a positive dependence on RH, with an explosive increase of OC_{sec} after RH exceeded 80%. Only 6% of the 2018–2019 samples (10 out of 180) experienced such humid conditions, whereas this fraction was as high as 37% for 2019–2020 (corresponding to 42 out of the 112 samples). Therefore, the inter-annual variation of OC_{sec} was likely associated with the different RH levels between the two campaigns. Although the daily average temperatures could drop to below $-20\text{ }^{\circ}\text{C}$ during the measurement periods, simulation results based on the ISORROPIA-II thermodynamic model (Guo et al., 2017a; Song et al., 2018; see Supplement for details) still showed considerable amounts of liquid water in aerosol phase at high RH, e.g., typically with AWC levels of above $50\text{ }\mu\text{g}/\text{m}^3$ when RH exceeded 80% (Figure 3). Therefore, heterogeneous reactions were presumably at play in the RH-dependent increase of OC_{sec} .~~

~~Figure 4 compares OC source apportionment results across different RH ranges ($< 60\%$, $60\text{--}80\%$ and $> 80\%$), which are termed low-, medium- and high-RH conditions, respectively, for the 2019–2020 campaign. Both OC_{sec} and its contribution to OC (f_{sec}) increased significantly from the low- through high-RH conditions, by factors of 9.8 and 2.6, respectively. Although the 2019–2020 campaign experienced much lower ambient temperatures compared to Beijing's winter ($\sim 0\text{ }^{\circ}\text{C}$), the~~

~~f_{sec} of Harbin reached 42% for the RH range of > 80%, generally comparable with the typical range of oxygenated organic aerosol (OOA) contribution (~35–60%) determined under humid winter conditions in Beijing (Sun et al., 2013, 2014, 2018; Hu et al., 2016; Xu et al., 2019).~~

The OC to EC ratio (OC/EC) is also a commonly used indicator for SOA, giving rise to the EC-tracer method for the estimation of OC_{sec} mass. However, it has long been recognized that SOA formation is usually not the only factor that can increase OC/EC, and another factor that could be playing a crucial role is the biomass smoke with relatively high emission ratios of OC to EC. Among the three primary factors resolved in this study, OC/EC for the primary emissions of BB-1 (extremely high as negligible EC was apportioned to this factor; Figure S4) and BB-2 (3.5) were both larger than that of non-BB_{pri} (2.8). Thus the influences of not only SOA but also biomass burning emissions need to be considered when interpreting the observed OC/EC. For the 2018–2019 campaign, the temporal variation of OC/EC was mainly driven by biomass burning emissions (especially the BB-1 factor), as can be seen from the positive dependence of OC/EC on levoglucosan and the comparison of OC/EC across the three cases with increasing LG/OC (Figure S7). In this case, the EC-tracer method should be used with caution, since the basic assumption, i.e., variation of OC/EC can be attributed primarily to SOA formation, was invalid. Unlike 2018–2019, SOA was the dominant driver for the variation of OC/EC during the 2019–2020 measurement period, as indicated by the positive dependence of OC/EC on sulfate and the comparison of OC/EC across the low- through high-RH conditions (Figure S8). During the 2019–2020 campaign, similar patterns of temporal variation were observed for OC_{sec} retrieved using the EC-tracer method and PMF approach, and both results supported the RH-dependent increase of OC_{sec} (Figure S9). However, compared to the PMF-based f_{sec} , the EC-tracer method resulted in a higher contribution of OC_{sec} to OC for the

high-RH conditions (60% vs. 42%). This is not surprising, as variation of biomass burning emissions could also contribute to the elevated OC/EC of the high-RH conditions (Figure S8), but this contribution could not be distinguished from that of SOA by the EC-tracer method. Nonetheless, enhanced SOA formation was evident for the high-RH conditions, which mainly occurred within the coldest months (December and January) during the 2019–2020 measurement period.

3.3 Variation of secondary inorganic aerosol

Both sulfate and SOR exhibited increasing trends as RH became higher (Figure 5), e.g., SOR averaged 0.09 ± 0.04 and 0.20 ± 0.07 for the RH ranges of below and above 80%, respectively. The apparent increase of SOR after RH exceeded 80% pointed to enhanced sulfate formation, presumably through heterogeneous reactions given the high AWC levels (as can be seen from Figure 3). In addition, NO_2 appeared to be at play in the heterogeneous conversion of SO_2 to sulfate, because the RH-dependent increase of SOR was more significant for the samples with relatively high NO_2 concentrations (e.g., above $30 \mu\text{g}/\text{m}^3$; Figure 6). Based on the observational results available, however, it was inconclusive whether NO_2 was the dominant oxidant for the heterogeneous formation of sulfate. Simulation results by ISORROPIA-II suggested moderately acidic aerosols (pH of 4.2 ± 1.1) for the high-RH conditions, and the importance of other oxidants (e.g., H_2O_2) could be comparable with or even overwhelm NO_2 for the oxidation of SO_2 in aerosol water at such pH levels (Guo et al., 2017b; Liu et al., 2017; Ye et al., 2018; Wang et al., 2021b). Nonetheless, the relationship between SOR and RH observed in Harbin was in general consistent with the wintertime results from Beijing. However, the threshold RH for sharp increase of SOR was higher in Harbin (80%) than that in Beijing ($\sim 40\text{--}70\%$), and the SOR in Harbin with RH above 80% (averaging 0.2) were at the lower end of ~~these~~ the corresponding values observed during winter in

Beijing (typically with averages of $\sim 0.2\text{--}0.6$) (Sun et al., 2013; Zheng et al., 2015b; Zhang et al., 2018; Li et al., 2019a; Liu et al., 2020b). ~~These differences indicated that heterogeneous formation of sulfate was less efficient in this study, and a likely cause~~ A likely cause for these differences was the relatively low temperatures during the measurement period, which would reduce the rate coefficients of relevant aqueous-phase reactions (Cheng et al., 2016).

The 2018–2019 and 2019–2020 campaigns exhibited comparable sulfate concentrations for the RH range of below 80%, with median values of 3.72 and $3.39\text{ }\mu\text{g}/\text{m}^3$, respectively (Figure S10). RH-dependent increase of sulfate was evident for both campaigns but was less significant for the former one, e.g., the median sulfate were 5.32 and $15.84\text{ }\mu\text{g}/\text{m}^3$ for the high-RH conditions of 2018–2019 and 2019–2020, respectively. As mentioned earlier, only 10 out of the 180 samples from the 2018–2019 campaign fell into the high-RH conditions. Among these 10 samples, the RH-dependent increase of sulfate was observed for only three ones with NO_2 concentrations of above $60\text{ }\mu\text{g}/\text{m}^3$, but was not evident for the remaining samples which had much lower NO_2 (mostly below $30\text{ }\mu\text{g}/\text{m}^3$; Figure 7). For the 2019–2020 campaign, however, the majority of the samples with RH above 80% showed NO_2 concentrations of above $60\text{ }\mu\text{g}/\text{m}^3$, accompanied with elevated sulfate. Therefore, the different NO_2 levels under high-RH conditions between the two campaigns (with median concentrations of 21.27 and $72.41\text{ }\mu\text{g}/\text{m}^3$ during 2018–2019 and 2019–2020, respectively; Figure S11) was a likely cause of the more significant RH-dependent increase of sulfate observed during the 2019–2020 campaign.

The 2019–2020 campaign also exhibited more significant RH-dependent increase of nitrate, similar to sulfate (Figure S12). In addition, an obvious difference between the two campaigns was that the nitrate to sulfate ($\text{NO}_3^-/\text{SO}_4^{2-}$) ratios tended to be higher during 2019–2020 (Figure

S13), with an average of 1.28 ± 0.51 (compared to 1.10 ± 0.66 for 2018–2019). This trend was somewhat surprising, as the 2019–2020 measurement period experienced substantially lower temperatures than 2018–2019 (Figure S13) and consequently was expected to be impacted by stronger heating-induced coal combustion emissions, which were a large source of SO₂. However, SO₂ were actually lower for the 2019–2020 campaign, presumably due to the implementation of clean air actions targeting pollutants from coal combustion. On the other hand, NO₂ were higher during 2019–2020. Factors responsible for this increase were unclear, while a possible explanation was that the meteorological conditions of 2019–2020 were generally less favorable for dispersion of air pollutions, as indicated by the frequent occurrences of high RH. In this case, the decrease of SO₂ ~~emission~~ emissions in 2019–2020 was inferred to be more significant after accounting for the unfavorable meteorological conditions. In general, the 2019–2020 campaign exhibited higher NO₂ to SO₂ ratios (Figure S13), which were in line with the observed variation of nitrate to sulfate ratios.

In addition to the relative abundances of NO₂ and SO₂, the influence of their gas-to-particle conversion ratios should also be considered when comparing NO₃⁻/SO₄²⁻ across different conditions. The two campaigns differed with respect to humidity levels and biomass burning emissions, both of which could influence SNA formation. Although NOR and SOR were indeed influenced by RH, NO₃⁻/SO₄²⁻ did not show clear dependence on RH (Figure S14). In addition, there were observational evidences indicating that biomass burning emissions could enhance photochemical oxidation of NO₂ whereas this effect was much weaker for SO₂ (Akagi et al., 2012; Collier et al., 2016), i.e., stronger BB impacts favor the increase of NO₃⁻/SO₄²⁻. Therefore, the larger NO₃⁻/SO₄²⁻ during the 2019–2020 campaign could not be explained by the reduced BB influences or the elevated RH levels, and instead should be attributed primarily to the higher NO₂ to SO₂ ratios. The

increasing trend of NO_2/SO_2 observed in this study was consistent with inventory results which typically indicated a more rapid decrease of SO_2 emissions compared to NO_2 during recent years in China (Zheng et al., 2018).

3.4 Variation of aerosol composition

The discussions above indicated significant differences between the two campaigns regarding the characteristics of both primary emissions and secondary aerosol formation. This in turn resulted in substantially different aerosol compositions between the two measurement periods, with the dominant drivers for the variation of aerosol composition being different as well (Figure 8).

For the 2018–2019 campaign, the contribution of OA to $(\text{PM}_{2.5})^*$ was much higher than that of SNA (60 vs. 28%). The variation of $(\text{PM}_{2.5})^*$ composition was driven mainly by biomass burning emissions (especially those from agricultural fires), which tended to increase the OA contribution and correspondingly decrease the relative abundance of SNA. During the most intensive BB episodes (with LG/OC above 3.0%), the OA contribution reached 66% whereas the SNA contribution dropped to 23%. For the 2019–2020 campaign, however, the contribution of SNA to $(\text{PM}_{2.5})^*$ was largely comparable with OA (41 vs. 49%), and heterogeneous chemistry became the dominant driver for the variation of $(\text{PM}_{2.5})^*$ composition. The relative abundances of both SNA and SOA increased considerably from the low-RH through high-RH conditions, with their total contributions reaching 62% for the RH range of above 80%.

During the 2019–2020 measurement period, significantly higher levels of major secondary ions were observed than 2018–2019, i.e., the total concentrations of sulfate, nitrate and ammonium (SNA) averaged 27.30 and 15.53 $\mu\text{g}/\text{m}^3$, respectively. This difference was largely explained by the RH-dependence. For the 2019–2020 campaign, the sampling events with RH above 80% were mainly

encountered in January of 2020 ($N = 20$) as well as in December of 2019 ($N = 17$), when the daily average temperatures were typically below -10°C . The frequent occurrences of high RH were uncommon for Harbin's winter, as can be seen from the comparison of RH in January across the past twenty years (Figure 9). Thus, the 2019–2020 campaign provided a unique opportunity to explore heterogeneous chemistry in Chinese cities located in the severe cold climate region, and might be considered as an upper limit regarding the RH-dependent enhancement of secondary aerosols. On the other hand, the effective increase of SNA and SOA under high-RH conditions implied the abundances of gaseous precursors, both organic and inorganic. To avoid the occurrence of extreme pollution events, a more fundamental solution would point to the effective control of gaseous pollutants.

3.5 Agricultural fires missed by the 2019–2020 campaign

The 2019–2020 campaign was designed to cover the entire heating season but was interrupted by the outbreak of COVID-19. Although there was no observational result on aerosol composition after 5 February, 2020, a severe $\text{PM}_{2.5}$ episode caused by agricultural fires was identified during 17–18 April, 2020, as indicated by the intensive fire counts recorded for Harbin and the surrounding areas (Figure 10). According to the open-access air quality data, the 24-hour $\text{PM}_{2.5}$ in Harbin reached ~ 500 and $900\ \mu\text{g}/\text{m}^3$ on these two days, respectively, with the hourly concentrations peaking at $\sim 2350\ \mu\text{g}/\text{m}^3$. During this period, similarly high $\text{PM}_{2.5}$ levels were observed for a nearby city, Suihua, which is located in the same region (the Song-Nen Plain) as Harbin. Based on a synthesis of air quality data and air mass trajectory, we found that the massive amounts of air pollutants in the Harbin-Suihua region, which were emitted by the agricultural fires within a concentrated period of two days, could be transported ~ 500 km northward to Heihe, a city located on the border between

China and Russia. As shown in Figures 10 and S15, $\text{PM}_{2.5}$ in Heihe started to increase when the back trajectory suggested air masses passing over the Harbin-Suihua region, resulting in an episode with a peak $\text{PM}_{2.5}$ concentration of $\sim 310 \mu\text{g}/\text{m}^3$. The discussions above indicated that although agricultural fires were not evident during the 2019–2020 measurement period, they were postponed to late April of 2020. Thus, agricultural fires were not actually eliminated by the toughest-ever policy on open burning, but broke out within a short period before the planting of crops in spring instead. It is noteworthy that the intensive open burning activities resulted in not only off-the-chart air pollutions for the nearby cities but also heavily-polluted episodes for downwind regions far away from the source areas. We suggest that transboundary transport of agricultural fire emissions from the Northeast Plain, especially the two provinces of Heilongjiang and Jilin, deserves more attention.

4. Conclusions and implications

Significant differences were observed between aerosol properties measured during two sequential heating seasons in the central city of the HC metropolitan area, i.e., Harbin. Briefly, the differences were caused by ~~inter-annual~~ inter-campaign variations of both primary emissions and secondary aerosol formation. The 2018–2019 measurement period was characterized by (i) frequent occurrences of agricultural fires, which were boosted by the “legitimate burning” policy, and (ii) overall low RH levels which were unfavorable for heterogeneous formation of secondary aerosols. Correspondingly, the observed $(\text{PM}_{2.5})^*$ was dominated by organic aerosol, with a substantially higher contribution than SNA (60 vs. 28%). Biomass burning emissions were the largest OC source for this measurement period. The BB to OC contribution (f_{BB}) was 46% before the onset of “legitimate burning” primarily due to household burning of crop residues, and increased to 59% after the onset of “legitimate burning” with the major contribution from agricultural fire emissions.

In addition to OC, the temporal variations of $(\text{PM}_{2.5})^*$ mass concentration and chemical composition were mainly driven by biomass burning as well, especially by agricultural fires. The average $(\text{PM}_{2.5})^*$ reached $\sim 100 \mu\text{g}/\text{m}^3$ for the most intensive BB episodes, with an enhanced OA contribution of 66% and a reduced SNA contribution of 23%.

Compared to 2018–2019, the 2019–2020 campaign was influenced by (i) a transition of open burning policy, i.e., agricultural fires were strictly prohibited, and (ii) frequent occurrences of high-RH conditions. In this case, no evidence was observed to indicate apparent influence of agricultural fires, and correspondingly, the f_{BB} (39%) was dominated by household burning of crop residues. In addition, both SNA and secondary OC (OC_{sec}) exhibited significant RH-dependent increases. For the RH range of above 80%, SOR and the OC_{sec} to OC contribution reached 0.2 and 42%, respectively, despite the low ambient temperatures encountered (averaging about -16°C in terms of daily average). Unlike 2018–2019, organic aerosol and SNA showed comparable contributions to $(\text{PM}_{2.5})^*$ for the 2019–2020 campaign (49 vs. 41%), and the variations of $(\text{PM}_{2.5})^*$ during this measurement period were mainly driven by secondary components.

5. Implications

This study has crucial implications for further improving the air quality in HC region. First, f_{BB} remained relatively high for the heating season of Harbin (e.g., compared to the wintertime results from Beijing), even without apparent influence of agricultural fires. This highlights the importance of reducing domestic use of crop residues, on top of previous clean air actions implemented for the residential sector primarily focusing on coal combustion. Second, driven by the transition of open burning policy, agricultural fires exhibited different patterns but were never eliminated. For example, although there was no “legitimate burning” period during 2019–2020 and agricultural fires did not

occur as frequently as during 2018–2019, burning did break out in spring of 2020 before crop planting. Thus, neither the “legitimate burning” policy released in 2018 nor the toughest-ever “strict prohibition” policy released in 2019 could be considered successful for the effective control of agricultural fires. More studies are necessary to design a new roadmap towards sustainable use of crop residues in Northeast China, which may contribute to the dual targets of air quality improvement and climate change mitigation. Third, it is noteworthy that $(\text{PM}_{2.5})^*$ averaged $\sim 115 \mu\text{g}/\text{m}^3$ for the high-RH conditions of 2019–2020, even higher than results from the most intensive BB episodes during 2018–2019. This reveals the need for effective control of gaseous precursors, both organic and inorganic, of secondary aerosols. Given the increasing trends of NO_2/SO_2 and $\text{NO}_3^-/\text{SO}_4^{2-}$ observed between 2018 and 2020, control of the NO_2 -related sources should be strengthened.

It should be noted that the discussions on heterogeneous formation of SOA and SNA did not necessarily exclude the reactions in fog/cloud water. Actually, based on the observational results available, we could not robustly distinguish the relative importance of various aqueous-phases pathways for secondary aerosol formation. To address this problem, air quality modeling with a focus on HC should be conducted in future studies, which could also quantitatively evaluate the contributions of various factors (e.g., meteorology, emissions and regional transport) to long-term trends of $\text{PM}_{2.5}$ concentration and chemical composition. An essential precondition is that the model could properly re-produce the observational results, which appears a substantial challenge for Harbin as indicated by the limited inter-comparison studies, especially for the periods with intensive agricultural fires or high RH levels (Cheng et al., 2021b).

Data availability.

Data are available from the corresponding author upon request (jiuemengliu@hit.edu.cn).

Author contribution

YC and JL designed the study and prepared the paper with inputs from all the coauthors. QY, XC, YZ, ZD and LL carried out the experiments. GG provided the air quality data. WM and HQ participated in the field campaign and data analysis. QZ and KB supervised the study.

Competing interests.

The authors declare that they have no conflict of interest.

Acknowledgements

This work was supported by the National Natural Science Foundation of China (41805097), the Natural Science Foundation of Heilongjiang Province (YQ2019D004), the State Key Laboratory of Urban Water Resource and Environment (2020DX14), the State Key Joint Laboratory of Environment Simulation and Pollution Control (19K02ESPCT), the State Environmental Protection Key Laboratory of Sources and Control of Air Pollution Complex (SCAPC202002) and Heilongjiang Touyan Team.

References

- Akagi, S. K., Craven, J. S., Taylor, J. W., McMeeking, G. R., Yokelson, R. J., Burling, I. R., Urbanski, S. P., Wold, C. E., Seinfeld, J. H., Coe, H., Alvarado, M. J., and Weise, D. R.: Evolution of trace gases and particles emitted by a chaparral fire in California, *Atmos. Chem. Phys.*, 12, 1397–1421, 2012.
- Cao, F., Zhang, S. C., Kawamura, K., and Zhang, Y. L.: Inorganic markers, carbonaceous components and stable carbon isotope from biomass burning aerosols in Northeast China, *Sci. Total Environ.*, 572, 1244–1251, 2016.
- Cheng, Y., Yu, Q. Q., Liu, J. M., Du, Z. Y., Liang, L. L., Geng, G. N., Zheng, B., Ma, W. L., Qi, H., Zhang, Q., and He, K.B.: Strong biomass burning contribution to ambient aerosol during heating season in a megacity in Northeast China: effectiveness of agricultural fire bans?, *Sci.*

550 *Total Environ.*, 754, 142144, 2021a.

551 Cheng, Y., Yu, Q. Q., Liu, J. M., Zhu, S. Q., Zhang, M. Y., Zhang, H. L., Zheng, B., and He, K. B.:
 552 Model vs. observation discrepancy in aerosol characteristics during a half-year long campaign
 553 in Northeast China: the role of biomass burning, *Environ. Pollut.*, 269, 116167, 2021b.

554 Cheng, Y. F., Zheng, G. J., Wei, C., Mu, Q., Zheng, B., Wang, Z. B., Gao, M., Zhang, Q., He, K. B.,
 555 Carmichael, G., Pöschl, U., and Su, H.: Reactive nitrogen chemistry in aerosol water as a
 556 source of sulfate during haze events in China, *Sci. Adv.*, 2, e1601530, 2016.

557 Collier, S., Zhou, S., Onasch, T. B., Jaffe, D. A., Kleinman, L., Sedlacek, A. J., Briggs, N. L., Hee,
 558 J., Fortner, E., Shilling, J. E., Worsnop, D., Yokelson, R. J., Parworth, C., Ge, X. L., Xu, J. Z.,
 559 Butterfield, Z., Chand, D., Dubey, M. K., Pekour, M. S., Springston, S., and Zhang, Q.:
 560 Regional influence of aerosol emissions from wildfires driven by combustion efficiency:
 561 insights from the BBOP campaign, *Environ. Sci. Technol.*, 50, 8613–8622, 2016.

562 Department of Ecology and Environment of Heilongjiang Province: Interim Provisions of
 563 Heilongjiang Province on Reward and Punishment for Straw Open Burning Management,
 564 available at: http://www.gov.cn/xinwen/2018-09/15/content_5322298.htm (last access: June
 565 17, 2021), 2018.

566 Fountoukis, C., and Nenes, A.: ISORROPIA II: a computationally efficient thermodynamic
 567 equilibrium model for $K^+-Ca^{2+}-Mg^{2+}-NH_4^+-Na^+-SO_4^{2-}-NO_3^- -Cl^- -H_2O$ aerosols, *Atmos.*
 568 *Chem. Phys.*, 7, 4639–4659, 2007.

569 Guo, H. Y., Liu, J. M., Froyd, K. D., Roberts, J. M., Veres, P. R., Hayes, P. L., Jimenez, J. L., Nenes,
 570 A., and Weber, R. J.: Fine particle pH and gas–particle phase partitioning of inorganic species
 571 in Pasadena, California, during the 2010 CalNex campaign, *Atmos. Chem. Phys.*, 17, 5703–
 572 5719, 2017a.

573 Guo, H. Y., Weber, R. J., and Nenes, A.: High levels of ammonia do not raise fine particle pH
 574 sufficiently to yield nitrogen oxide-dominated sulfate production, *Sci. Rep.*, 7, 12109, 2017b.

575 Hu, W. W., Hu, M., Hu, W., Jimenez, J. L., Yuan, B., Chen, W. T., Wang, M., Wu, Y. S., Chen, C.,
 576 Wang, Z. B., Peng, J. F., Zeng, L. M., and Shao, M.: Chemical composition, sources, and aging
 577 process of submicron aerosols in Beijing: contrast between summer and winter, *J. Geophys.*
 578 *Res. Atmos.*, 121, 1955–1977, 2016.

579 Huang, X., Ding, A. J., Gao, J., Zheng, B., Zhou, D. R., Qi, X. M., Tang, R., Wang, J. P., Ren, C.

H., Nie, W., Chi, X. G., Xu, Z., Chen, L. D., Li, Y. Y., Che, F., Pang, N., Wang, H. K., Tong, D., Qin, W., Cheng, W., Liu, W. J., Fu, Q. Y., Liu, B. X., Chai, F. H., Davis, S. J., Zhang, Q., and He, K. B.: Enhanced secondary pollution offset reduction of primary emissions during COVID-19 lockdown in China, *Natl. Sci. Rev.*, 8, nwaa137, 2021.

Kuang, Y., He, Y., Xu, W. Y., Yuan, B., Zhang, G., Ma, Z. Q., Wu, C. H., Wang, C. M., Wang, S. H., Zhang, S. Y., Tao, J. C., Ma, N., Su, H., Cheng, Y. F., Shao, M., and Sun, Y. L.: Photochemical aqueous-phase reactions induce rapid daytime formation of oxygenated organic aerosol on the North China Plain, *Environ. Sci. Technol.*, 54, 3849–3860, 2020.

Le, T. H., Wang, Y., Liu, L., Yang, J. N., Yung, Y. L., Li, G. H., and Seinfeld, J. H.: Unexpected air pollution with marked emission reductions during the COVID-19 outbreak in China, *Science*, 369, 702–706, 2020.

Li, H. Y., Cheng, J., Zhang, Q., Zheng, B., Zhang, Y. X., Zheng, G. J., and He, K. B.: Rapid transition in winter aerosol composition in Beijing from 2014 to 2017: response to clean air actions, *Atmos. Chem. Phys.*, 19, 11485–11499, 2019a.

Li, Y. C., Liu, J., Han, H., Zhao, T. L., Zhang, X., Zhuang, B. L., Wang, T. J., Chen, H. M., Wu, Y., and Li, M. M.: Collective impacts of biomass burning and synoptic weather on surface PM_{2.5} and CO in Northeast China, *Atmos. Environ.*, 213, 64–80, 2019b.

Liu, J. M., Wang, P. F., Zhang, H. L., Du, Z. Y., Zheng, B., Yu, Q. Q., Zheng, G. J., Ma, Y. L., Zheng, M., Cheng, Y., Zhang, Q., and He, K. B.: Integration of field observation and air quality modeling to characterize Beijing aerosol in different seasons, *Chemosphere*, 242, 125195, 2020a.

Liu, J. M., Alexander, L., Fast, J. D., Lindenmaier, R., Shilling, J. E.: Aerosol characteristics at the Southern Great Plains site during the HI-SCALE campaign, *Atmos. Chem. Phys.*, 21, 5101–5116, 2021a.

Liu, P. F., Ye, C., Xue, C. Y., Zhang, C. L., Mu, Y. J., and Sun, X.: Formation mechanisms of atmospheric nitrate and sulfate during the winter haze pollution periods in Beijing: gas-phase, heterogeneous and aqueous-phase chemistry, *Atmos. Chem. Phys.*, 20, 4153–4165, 2020b.

Liu, T. Y., Chan, A. W. H., and Abbatt, J. P. D.: Multiphase oxidation of sulfur dioxide in aerosol particles: implications for sulfate formation in polluted environments, *Environ. Sci. Technol.*, 8, 4227–4242, 2021b.

610 Lv, Z. F., Wang, X. T., Deng, F. Y., Ying, Q., Archibald, A. T., Jones, R. L., Ding, Y., Cheng, Y., Fu,
 611 M. L., Liu, Y., Man, H. Y., Xue, Z. G., He, K. B., Hao, J. M., and Liu, H.: Source-receptor
 612 relationship revealed by the halted traffic and aggravated haze in Beijing during the COVID-
 613 19 lockdown, *Environ. Sci. Technol.*, 54, 15660–15670, 2020.

614 May, A. A., McMeeking, G. R., Lee, T., Taylor, J. W., Craven, J. S., Burling, I., Sullivan, A. P.,
 615 Akagi, S., Collett, J. L., Flynn, M., Coe, H., Urbanski, S. P., Seinfeld, J. H., Yokelson, R. J.,
 616 and Kreidenweis, S. M.: Aerosol emissions from prescribed fires in the United States: a
 617 synthesis of laboratory and aircraft measurements, *J. Geophys. Res. Atmos.*, 119, 11826–11849,
 618 2014.

619 McClure, C. D., Lim, C. Y., Hagan, D. H., Kroll, J. H., Cappa, C. D.: Biomass-burning-derived
 620 particles from a wide variety of fuels – Part 1: properties of primary particles, *Atmos. Chem.*
 621 *Phys.*, 20, 1531–1547, 2020.

622 McMeeking, G. R., Kreidenweis, S. M., Baker, S., Carrico, C. M., Chow, J. C., Collett, J. L., Hao,
 623 W. M., Holden, A. S., Kirchstetter, T. W., Malm, W. C., Moosmüller, H., Sullivan, A. P., and
 624 Wold, C. E.: Emissions of trace gases and aerosols during the open combustion of biomass in
 625 the laboratory, *J. Geophys. Res.*, 114, D19210, 2009.

626 National Bureau of Statistics of China: China Statistical Yearbook 2020, available at:
 627 <http://www.stats.gov.cn/tjsj/ndsj/2020/indexeh.htm>, 2020.

628 Pokhrel, R. P., Wagner, N. L., Langridge, J. M., Lack, D. A., Jayarathne, T., Stone, E. A., Stockwell,
 629 C. E., Yokelson, R. J., and Murphy, S. M.: Parameterization of single-scattering albedo (SSA)
 630 and absorption Ångström exponent (AAE) with EC/OC for aerosol emissions from biomass
 631 burning, *Atmos. Chem. Phys.*, 16, 9549–9561, 2016.

632 Shi, Z. B., Vu, T., Kotthaus, S., Harrison, R. M., Grimmond, S., Yue, S. Y., Zhu, T., Lee, J., Han, Y.
 633 Q., Demuzere, M., Dunmore, R. E., Ren, L. J., Liu, D., Wang, Y. L., Wild, O., Allan, J., Acton,
 634 W. J., Barlow, J., Barratt, B., Beddows, D., Bloss, W. J., Calzolari, G., Carruthers, D., Carslaw,
 635 D. C., Chan, Q., Chatzidiakou, L., Chen, Y., Crilley, L., Coe, H., Dai, T., Doherty, R., Duan, F.
 636 K., Fu, P. Q., Ge, B. Z., Ge, M. F., Guan, D. B., Hamilton, J. F., He, K. B., Heal, M., Heard, D.,
 637 Hewitt, C. N., Hollaway, M., Hu, M., Ji, D. S., Jiang, X. J., Jones, R., Kalberer, M., Kelly, F.
 638 J., Kramer, L., Langford, B., Lin, C., Lewis, A. C., Li, J., Li, W. J., Liu, H., Liu, J. F., Loh, M.,
 639 Lu, K. D., Lucarelli, F., Mann, G., McFiggans, G., Miller, M. R., Mills, G., Monk, P., Nemitz,

E., O'Connor, F., Ouyang, B., Palmer, P. I., Percival, C., Popoola, O., Reeves, C., Rickard, A. R., Shao, L. Y., Shi, G. Y., Spracklen, D., Stevenson, D., Sun, Y. L., Sun, Z. W., Tao, S., Tong, S. R., Wang, Q. Q., Wang, W. H., Wang, X. M., Wang, X. J., Wang, Z. F., Wei, L. F., Whalley, L., Wu, X. F., Wu, Z. J., Xie, P. H., Yang, F. M., Zhang, Q., Zhang, Y. L., Zhang, Y. H., and Zheng, M.: Introduction to the special issue “In-depth study of air pollution sources and processes within Beijing and its surrounding region (APHH-Beijing)”, *Atmos. Chem. Phys.*, 19, 7519–7546, 2019.

Shrivastava, M., Cappa, C. D., Fan, J. W., Goldstein, A. H., Guenther, A. B., Jimenez, J. L., Kuang, C., Laskin, A., Martin, S. T., Ng, N. L., Petaja, T., Pierce, J. R., Rasch, P. J., Roldin, P., Seinfeld, J. H., Shilling, J., Smith, J. N., Thornton, J. A., Volkamer, R., Wang, J., Worsnop, D. R., Zaveri, R. A., Zelenyuk, A., and Zhang, Q.: Recent advances in understanding secondary organic aerosol: implications for global climate forcing, *Rev. Geophys.*, 55, 509–559, 2017.

Song, S. J., Gao, M., Xu, W. Q., Shao, J. Y., Shi, G. L., Wang, S. X., Wang, Y. X., Sun, Y. L., and McElroy, M. B.: Fine-particle pH for Beijing winter haze as inferred from different thermodynamic equilibrium models, *Atmos. Chem. Phys.*, 18, 7423–7438, 2018.

Su, H., Cheng, Y. F., and Pöschl, U.: New multiphase chemical processes influencing atmospheric aerosols, air quality, and climate in the Anthropocene, *Acc. Chem. Res.*, 53, 2034–2043, 2020.

Sun, Y. L., Jiang, Q., Wang, Z. F., Fu, P. Q., Li, J., Yang, T., and Yin, Y.: Investigation of the sources and evolution processes of severe haze pollution in Beijing in January 2013, *J. Geophys. Res. Atmos.*, 119, 4380–4398, 2014.

Sun, Y. L., Wang, Z. F., Fu, P. Q., Jiang, Q., Yang, T., Li, J., and Ge, X. L.: The impact of relative humidity on aerosol composition and evolution processes during wintertime in Beijing, China, *Atmos. Environ.*, 77, 927–934, 2013.

Sun, Y. L., Xu, W. Q., Zhang, Q., Jiang, Q., Canonaco, F., Prévôt, A. S. H., Fu, P. Q., Li, J., Jayne, J., Worsnop, D. R., and Wang, Z. F.: Source apportionment of organic aerosol from 2-year highly time-resolved measurements by an aerosol chemical speciation monitor in Beijing, China, *Atmos. Chem. Phys.*, 18, 8469–8489, 2018.

Wang, G. H., Zhang, R. Y., Gomez, M. E., Yang, L. X., Zamora, M. L., Hu, M., Lin, Y., Peng, J. F., Guo, S., Meng, J. J., Li, J. J., Cheng, C. L., Hu, T. F., Ren, Y. Q., Wang, Y. S., Gao, J., Cao, J. J., An, Z. S., Zhou, W. J., Li, G. H., Wang, J. Y., Tian, P. F., Marrero-Ortiz, W., Secret, J., Du,

Z. F., Zheng, J., Shang, D. J., Zeng, L. M., Shao, M., Wang, W. G., Huang, Y., Wang, Y., Zhu, Y. J., Li, Y. X., Hu, J. X., Pan, B. W., Cai, L., Cheng, Y. T., Ji, Y. M., Zhang, F., Rosenfeld, D., Liss, P. S., Duce, R. A., Kolb, C. E., and Molina, M. J.: Persistent sulfate formation from London Fog to Chinese haze, *Proc. Natl. Acad. Sci. U.S.A.*, 113, 13630–13635, 2016.

Wang, J. F., Li, J. Y., Ye, J. H., Zhao, J., Wu, Y. Z., Hu, J. L., Liu, D. T., Nie, D. Y., Shen, F. Z., Huang, X. P., Huang, D. D., Ji, D. S., Sun, X., Xu, W. Q., Guo, J. P., Song, S. J., Qin, Y. M., Liu, P. F., Turner, J. R., Lee, H. C., Hwang, S., Liao, H., Martin, S. T., Zhang, Q., Chen, M. D., Sun, Y. L., Ge, X. L., and Jacob, D. J.: Fast sulfate formation from oxidation of SO₂ by NO₂ and HONO observed in Beijing haze, *Nat. Commun.*, 11, 2844, 2020a.

Wang, J. F., Ye, J. H., Zhang, Q., Zhao, J., Wu, Y. Z., Li, J. Y., Liu, D. T., Li, W. J., Zhang, Y. G., Wu, C., Xie, C. H., Qin, Y. M., Lei, Y. L., Huang, X. P., Guo, J. P., Liu, P. F., Fu, P. Q., Li, Y. J., Lee, H. C., Choi, H., Zhang, J., Liao, H., Chen, M. D., Sun, Y. L., Ge, X. L., Martin, S. T., and Jacob, D. J.: Aqueous production of secondary organic aerosol from fossil-fuel emissions in winter Beijing haze, *Proc. Natl. Acad. Sci. U. S. A.*, 118, e2022179118, 2021a.

Wang, P. F., Chen, K. Y., Zhu, S. Q., Wang, P., and Zhang, H. L.: Severe air pollution events not avoided by reduced anthropogenic activities during COVID-19 outbreak, *Resour. Conserv. Recy.*, 158, 104814, 2020b.

Wang, W. G., Liu, M. Y., Wang, T. T., Song, Y., Zhou, L., Cao, J. J., Hu, J. N., Tang, G. G., Chen, Z., Li, Z. J., Xu, Z. Y., Peng, C., Lian, C. F., Chen, Y., Pan, Y. P., Zhang, Y. H., Sun, Y. L., Li, W. J., Zhu, T., Tian, H. Z., and Ge, M. F.: Sulfate formation is dominated by manganese-catalyzed oxidation of SO₂ on aerosol surfaces during haze events, *Nat. Commun.*, 12, 1993, 2021b.

Wang, Y. J., Hu, M., Xu, N., Qin, Y. H., Wu, Z. J., Zeng, L. W., Huang, X. F., and He, L. Y.: Chemical composition and light absorption of carbonaceous aerosols emitted from crop residue burning: influence of combustion efficiency, *Atmos. Chem. Phys.*, 20, 13721–13734, 2020c.

Wang, Y. X., Zhang, Q. Q., Jiang, J. K., Zhou, W., Wang, B. Y., He, K. B., Duan, F. K., Zhang, Q., Philip, S., and Xie, Y. Y.: Enhanced sulfate formation during China's severe winter haze episode in January 2013 missing from current models, *J. Geophys. Res. Atmos.*, 119, 10425–10440, 2014.

Xu, W. Q., Sun, Y. L., Wang, Q. Q., Zhao, J., Wang, J. F., Ge, X. L., Xie, C. H., Zhou, W., Du, W.,

Li, J., Fu, P. Q., Wang, Z. F., Worsnop, D. R., and Coe, H.: Changes in aerosol chemistry from 2014 to 2016 in winter in Beijing: insights from high-resolution aerosol mass spectrometry, *J. Geophys. Res. Atmos.*, 124, 1132–1147, 2019.

Yang, T., Gbaguidi, A., Yan, P.Z., Zhang, W.D., Zhu, L.L., Yao, X.F., Wang, Z.F., Chen, H.: Model elucidating the sources and formation mechanisms of severe haze pollution over Northeast mega-city cluster in China, *Atmos. Environ.*, 230, 692–700, 2017.

Ye, C., Liu, P. F., Ma, Z. B., Xue, C. Y., Zhang, C. L., Zhang, Y. Y., Liu, J. F., Liu, C. T., Sun, X., and Mu, Y. J.: High H₂O₂ concentrations observed during haze periods during the winter in Beijing: importance of H₂O₂ oxidation in sulfate formation, *Environ. Sci. Technol. Lett.*, 5, 757–763, 2018.

Zhang, J., Liu, L., Xu, L., Lin, Q. H., Zhao, H. J., Wang, Z. B., Guo, S., Hu, M., Liu, D. T., Shi, Z. B., Huang, D., and Li, W. J.: Exploring wintertime regional haze in northeast China: role of coal and biomass burning, *Atmos. Chem. Phys.*, 20, 5355–5372, 2020.

Zhang, Q., Zheng, Y. X., Tong, D., Shao, M., Wang, S. X., Zhang, Y. H., Xu, X. D., Wang, J. N., He, H., Liu, W. Q., Ding, Y. H., Lei, Y., Li, J. H., Wang, Z. F., Zhang, X. Y., Wang, Y. S., Cheng, J., Liu, Y., Shi, Q. R., Yan, L., Geng, G. N., Hong, C. P., Li, M., Liu, F., Zheng, B., Cao, J. J., Ding, A. J., Gao, J., Fu, Q. Y., Huo, J. T., Liu, B. X., Liu, Z. R., Yang, F. M., He, K. B., and Hao, J. M.: Drivers of improved PM_{2.5} air quality in China from 2013 to 2017, *Proc. Natl. Acad. Sci. U. S. A.*, 116, 24463–24469, 2019.

Zhang, R., Sun, X. S., Shi, A. J., Huang, Y. H., Yan, J., Nie, T., Yan, X., Li, X.: Secondary inorganic aerosols formation during haze episodes at an urban site in Beijing, China, *Atmos. Environ.*, 177, 275–282, 2018.

Zheng, B., Tong, D., Li, M., Liu, F., Hong, C. P., Geng, G. N., Li, H. Y., Li, X., Peng, L. Q., Qi, J., Yan, L., Zhang, Y. X., Zhao, H. Y., Zheng, Y. X., He, K. B., and Zhang, Q.: Trends in China's anthropogenic emissions since 2010 as the consequence of clean air actions, *Atmos. Chem. Phys.*, 18, 14095–14111, 2018.

Zheng, B., Zhang, Q., Zhang, Y., He, K. B., Wang, K., Zheng, G. J., Duan, F. K., Ma, Y. L., and Kimoto, T.: Heterogeneous chemistry: a mechanism missing in current models to explain secondary inorganic aerosol formation during the January 2013 haze episode in North China, *Atmos. Chem. Phys.*, 15, 2031–2049, 2015a.

730 Zheng, G. J., Duan, F. K., Su, H., Ma, Y. L., Cheng, Y., Zheng, B., Zhang, Q., Huang, T., Kimoto,
731 T., Chang, D., Pöschl, U., Cheng, Y. F., and He, K.B.: Exploring the severe winter haze in
732 Beijing: the impact of synoptic weather, regional transport and heterogeneous reactions, *Atmos.*
733 *Chem. Phys.*, 15, 2969–2983, 2015b.

734 Zheng, G. J., Su, H., Wang, S. W., Andreae, M. O., Pöschl, U., and Cheng, Y. F.: Multiphase buffer
735 theory explains contrasts in atmospheric aerosol acidity, *Science*, 369, 1374–1377, 2020.

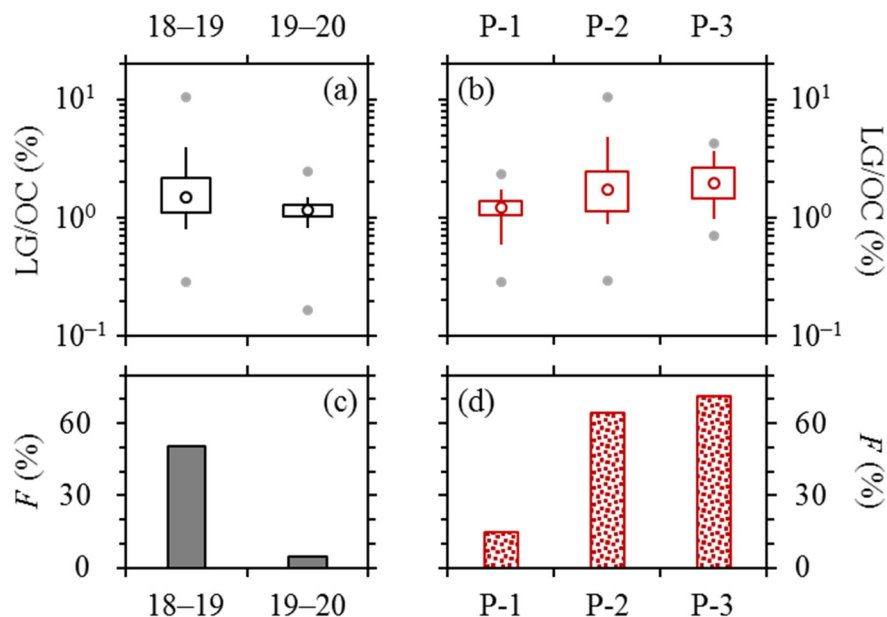


Figure 1. Comparisons of levoglucosan to OC ratios, i.e., LG/OC (on a basis of carbon mass), and the fractions of samples with LG/OC above 1.5% (denoted as F), **(a, c)** between the 2018–2019 and 2019–2020 campaigns, and **(b, d)** across the 2018–2019 samples collected before (P-1), during (P-2) and after (P-3) the “legitimate burning” periods. Lower and upper box bounds indicate the 25th and 75th percentiles, the whiskers below and above the box indicate the 5th and 95th percentiles, the solid circles below and above the box indicate the minimum and maximum, and the open circle within the box marks the median (the same hereinafter).

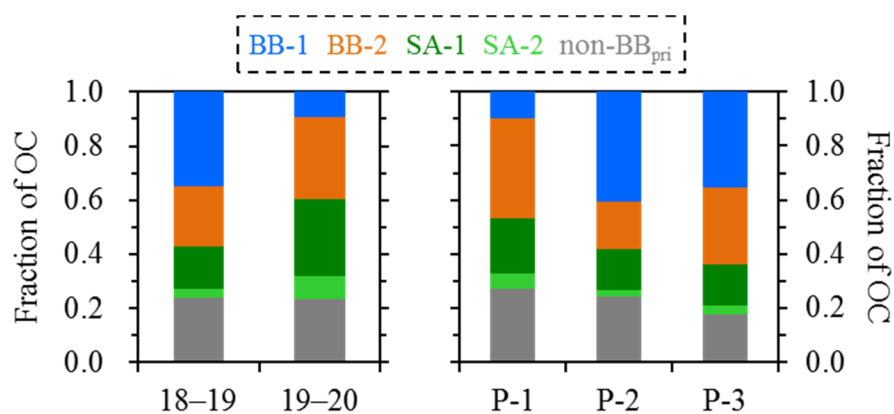


Figure 2. Comparison of OC source apportionment results between the 2018–2019 and 2019–2020 campaigns (left panel), and across the 2018–2019 samples collected before (P-1), during (P-2) and after (P-3) the “legitimate burning” periods (right panel).

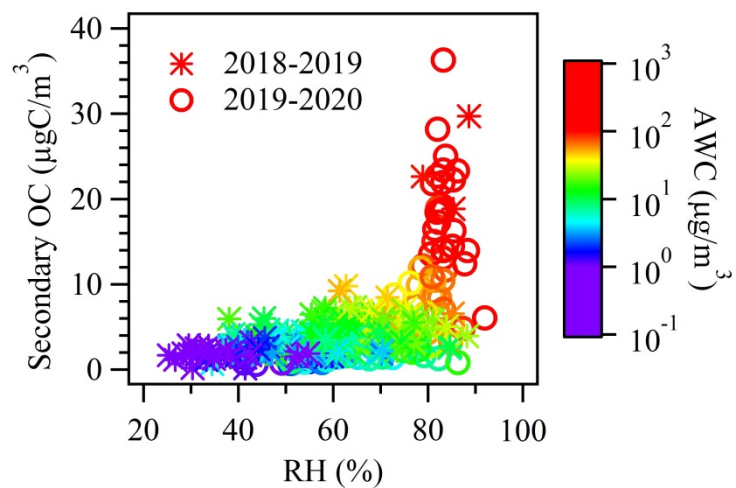


Figure 3. Dependence of secondary OC (OC_{sec}) on RH among the two campaigns, color-coded by AWC levels. Results from the 2018–2019 campaign and 2019–2020 campaign were marked using stars and circles, respectively. The majority of the data points with RH above 80% were observed during 2019–2020. RH exceeded 80% for only ten samples collected during 2018–2019, and only three out of these ten samples showed RH-dependent increase of OC_{sec} .

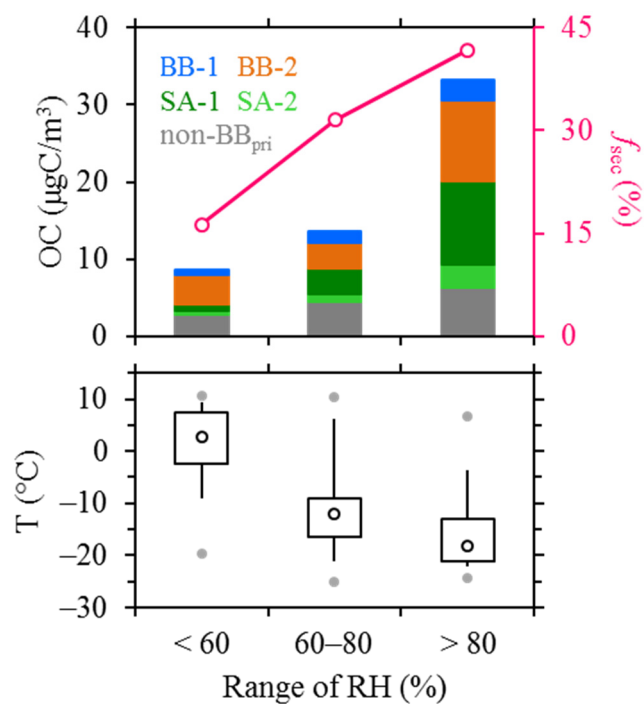


Figure 4. Comparisons of OC source apportionment results (upper panel, left axis), the contribution contributions of PMF-based OC_{sec} to OC (f_{sec} ; upper panel, right axis), and ambient temperatures across different RH ranges (lower panel) for the 2019–2020 campaign.

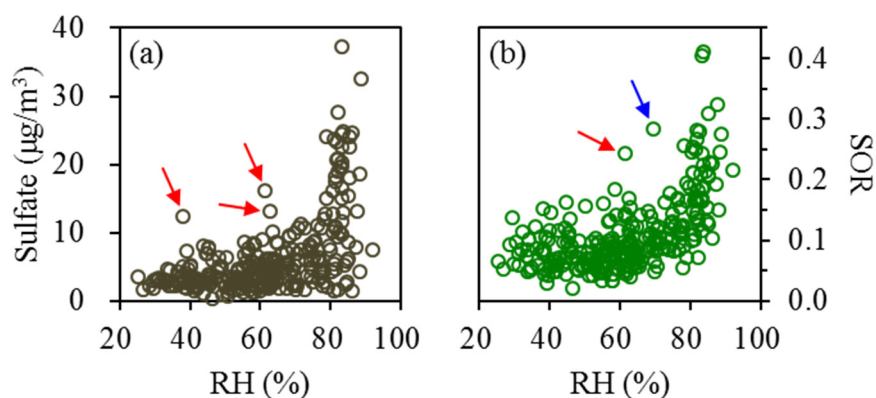


Figure 5. Dependences of (a) sulfate and (b) SOR on RH. Results from the 2018–2019 and 2019–2020 campaigns are combined. Relatively high sulfate are typically observed for the conditions with RH above 80%, which is also the case for SOR. There appear to be several outliers showing considerably higher sulfate or SOR than other samples at similar RH. All the outliers occurred during the 2018–2019 measurement period, and most of them were accompanied with extremely high levoglucosan concentrations (above $5 \mu\text{g}/\text{m}^3$), as highlighted by the red arrows. The outlier highlighted by the blue arrow was observed ~~with~~ at an ambient temperature of above 10°C , which was uncommon for the heating season. The outliers indicate that factors other than RH were also at play in sulfate formation, but the influences were evident for only several samples.

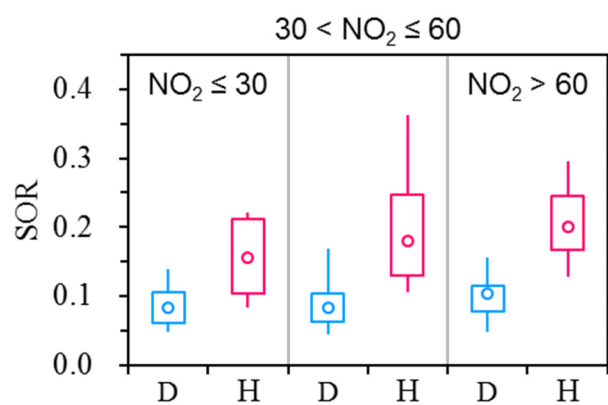


Figure 6. Comparisons of SOR between different RH levels, with results from different NO₂ ranges (below 30, 30–60 and above 60 µg/m³) shown separately. Results from both the 2018–2019 and 2019–2020 campaigns are included. The terms “D” and “H” indicate relatively dry (RH below 80%) and more humid conditions (RH above 80%), respectively.

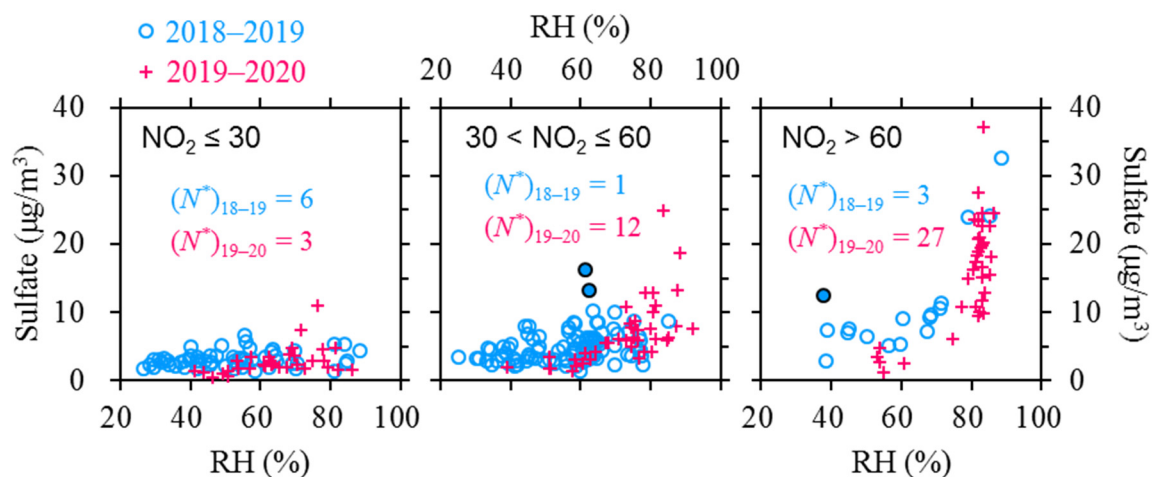
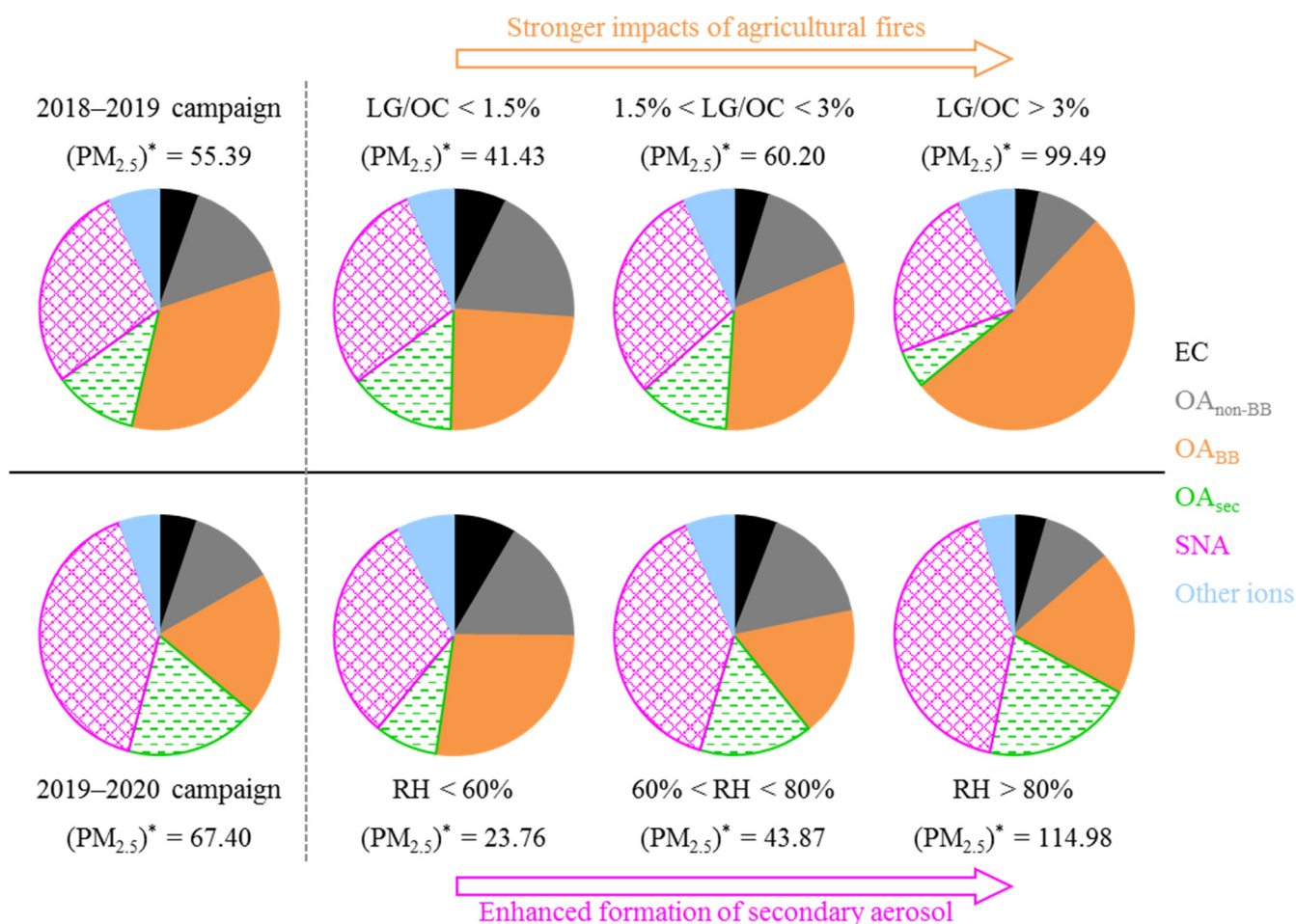


Figure 7. Dependences of sulfate on RH in different NO₂ ranges (below 30, 30–60 and above 60 μg/m³). Results from the 2018–2019 and 2019–2020 campaigns are shown using different markers. The outliers in Figure 5a are highlighted by the solid circles. *N*^{*} indicates the number of samples with RH above 80%. High-RH conditions were typically accompanied with NO₂ concentrations of below 30 μg/m³ during 2018–2019, and NO₂ above 60 μg/m³ during 2019–2020, respectively.



779

780 **Figure 8.** Comparison of aerosol compositions measured for the 2018–2019 and 2019–2020 campaigns. The 2018–
 781 2019 measurement period experienced relatively dry meteorological conditions (with RH levels rarely exceeding
 782 80%) and was characterized by a wide window of ~3 months for “legitimate burning”. Correspondingly, variations
 783 of $(PM_{2.5})^*$ concentration (in $\mu g/m^3$) and aerosol composition observed during 2018–2019 were mainly driven by
 784 agricultural fires. However, the “legitimate burning” policy was terminated in 2019, and the 2019–2020 campaign
 785 did not show clear evidence for apparent influence of agricultural fires. On the other hand, high-RH conditions
 786 occurred much more frequently during the 2019–2020 measurement period compared to 2018–2019.
 787 Correspondingly, variations of $(PM_{2.5})^*$ concentration and aerosol composition observed during 2019–2020 were
 788 mainly driven by RH-dependent increase of secondary aerosols.

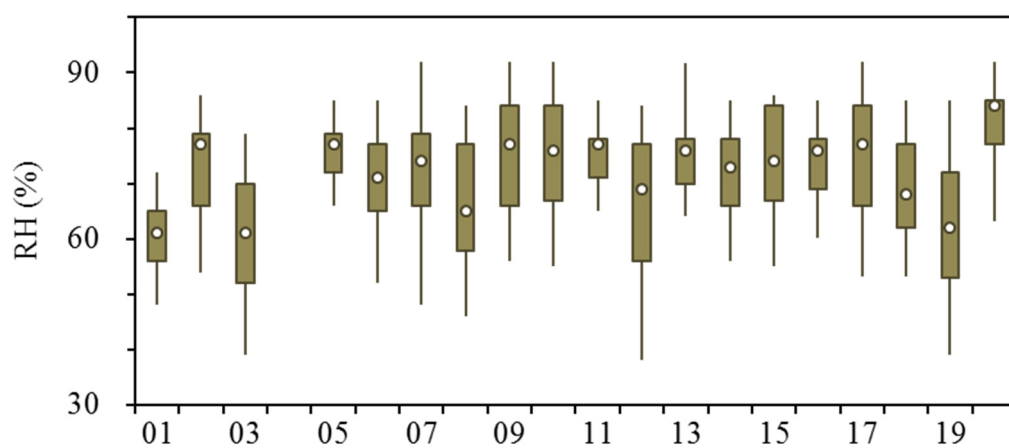


Figure 9. Comparison of RH measured during January in Harbin across the past twenty years (from 2001 through 2020). Time resolution is 1-h for the RH data. No observational result is available for January of 2004.

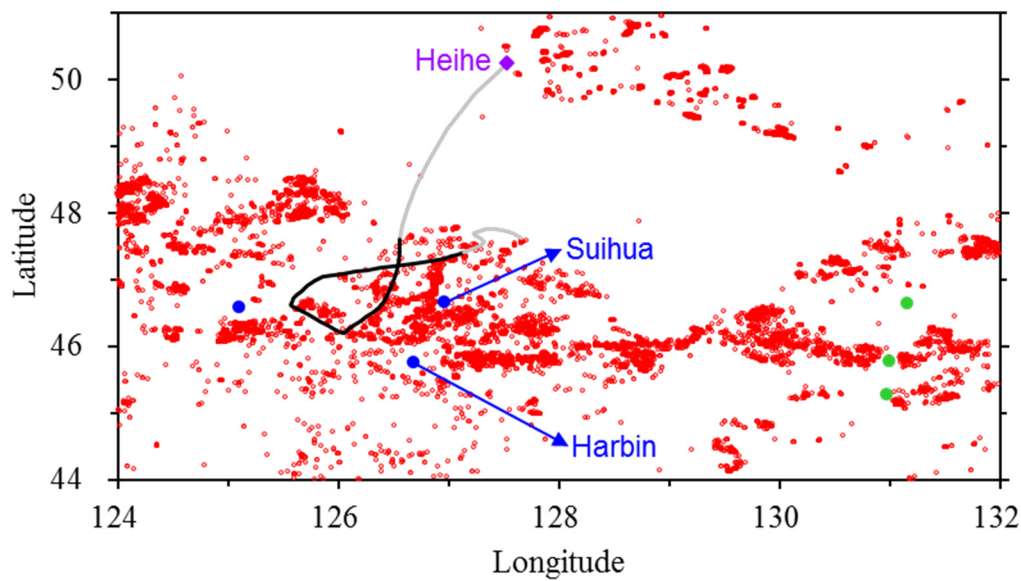


Figure 10. Active fires (red circles) detected by the joint NASA/NOAA Suomi-National Polar orbiting Partnership (S-NPP) satellite for Heilongjiang Province during 17–18 April, 2020. Three cities located in the Song-Nen Plain are shown using blue dots (the unlabeled city is Daqing), and three cities located in the San-Jiang Plain (i.e., Shuangyashan, Qitaihe and Jixi with decreasing latitudes) are shown using green dots. The two plains, separated by mountains, are the main agricultural regions in Heilongjiang. Intensive agricultural fires are evident for both plains during the two-day episode, indicating the open burning activities are province-wide, although prohibited. The agricultural fires resulted in severe $PM_{2.5}$ pollution for nearby cities, e.g., the 24-hour concentrations peaked at ~ 900 and $675 \mu g/m^3$ in Harbin and Jixi, respectively. A $PM_{2.5}$ episode was observed even for Heihe (~ 500 km away from Harbin) on 19 April, 2020, which was attributed to the pollutants transported from the Harbin-Suihua region. The solid line indicates the 72-hour back trajectory ending at 7:00 in Heihe, accompanied with the highest 1-hour $PM_{2.5}$ observed on 19 April, 2020 ($\sim 310 \mu g/m^3$). The trajectory indicates transport pathway of air masses impacting Heihe, with the segment in black showing locations of the air masses during 17–18 April, 2020.

Supporting Information for:

Dramatic changes in Harbin aerosol during 2018–2020: the roles of open burning policy and secondary aerosol formation

Yuan Cheng¹, Qin-qin Yu¹, Jiu-meng Liu^{1,*}, Xu-bing Cao¹, Ying-jie Zhong¹, Zhen-yu Du², Lin-lin Liang³, Guan-nan Geng⁴, Wan-li Ma¹, Hong Qi¹, Qiang Zhang⁵, Ke-bin He⁴

¹ State Key Laboratory of Urban Water Resource and Environment, School of Environment, Harbin Institute of Technology, Harbin, China

² National Research Center for Environmental Analysis and Measurement, Environmental Development Center of the Ministry of Ecology and Environment, Beijing, China

³ State Key Laboratory of Severe Weather & CMA Key Laboratory of Atmospheric Chemistry, Chinese Academy of Meteorological Sciences, Beijing, China

⁴ State Key Joint Laboratory of Environment Simulation and Pollution Control, School of Environment, Tsinghua University, Beijing, China

⁵ Department of Earth System Science, Tsinghua University, Beijing, China

* Corresponding author. Jiu-meng Liu (jiumengliu@hit.edu.cn).

~~SI-1. Field observation.~~

~~Two campaigns were conducted at an urban site in Harbin during the heating seasons of 2018–2019 (from 16 October, 2018 to 14 April, 2019; $N = 180$) and 2019–2020 (from 16 October, 2019 to 4 February, 2020; $N = 112$). The sampling was performed in the campus of Harbin Institute of Technology (45°45'24" N, 126°40'49" E), using a low volume sampler (MiniVol; Airmetrics, OR, USA) operated with pre-baked quartz fiber filters (2500 QAT-UP; Pall Corporation, NY, USA) at a flow rate of 5 L/min. As described in Cheng et al. (2021), the samples were analyzed for organic carbon (OC), elemental carbon (EC), organic tracers for biomass burning (levoglucosan and mannosan) and water-soluble inorganic ions. Briefly, OC and EC were measured by a thermal/optical carbon analyzer (DRI-2001; Atmoslytic Inc., CA, USA), using the IMPROVE-A temperature protocol with transmittance charring correction. Levoglucosan and mannosan were detected by a Dionex ion chromatography (IC) system (ICS-5000⁺; Thermo Fisher Scientific Inc., MA, USA), using the high performance anion-exchange chromatography coupled to pulsed amperometric detection (HPAEC-PAD) method. The IC was also used to determine the inorganic ions including sulfate, nitrate, ammonium, etc.~~

~~Hourly air quality data (e.g., CO), which were measured at a nearby monitoring site (Taiping Hongwei Park, about 2.4 km away from the filter sampling site) operated by the China National Environmental Monitoring Center (CNEMC), were obtained from China's National Urban Air Quality Real Time Publishing Platform (<http://106.37.208.233:20035/>). Hourly meteorological data including temperature and relative humidity were obtained from Weather Underground (<https://www.wunderground.com>).~~

~~SI-2. Aerosol water content (AWC) and aerosol pH estimated using ISORROPIA-II~~

~~To estimate AWC and aerosol pH during the two campaigns, ISORROPIA-II was run with daily integrated data (including concentrations of aerosol-phase species, ambient temperature and relative humidity) as input. To simplify the simulations, ISORROPIA-II was run assuming particles are “metastable”. It is also assumed that the particles are internally mixed and that pH does not vary with particle size (so that bulk properties represent the overall aerosol pH).~~

~~Because of limitations in input data, e.g., no gas phase data available directly on site, the calculation was done in two ways, the “reverse” and “forward” mode. For the “reverse” mode, the measured aerosol-phase data were deployed as input to retrieve AWC and pH directly. For the “forward” mode, the model was run in an “iteration” way, that we used the measured aerosol-phase data as initial input, ran ISORROPIA-II in the “forward” mode to predict gas-phase concentrations of NH_3 , HNO_3 and HCl , and used the sum of predicted gas-phase and measured aerosol-phase~~

concentrations as the input for next round. The calculations were repeated until the simulated results were stable and in line with the observational data. Both the reverse and forward modes showed comparable AWC levels (Figure S14). For pH, we specifically deployed results using the forward mode, as studies have suggested that the forward mode gives more accurate and robust results than the reverse mode (e.g., Guo et al., 2017, 2018; Song et al., 2018).

References

- Cheng, Y., Yu, Q.Q., Liu, J.M., Du, Z.Y., Liang, L.L., Geng, G.N., Zheng, B., Ma, W.L., Qi, H., Zhang, Q., and He, K.B.: Strong biomass burning contribution to ambient aerosol during heating season in a megacity in Northeast China: effectiveness of agricultural fire bans?, *Sci. Total Environ.*, 754, 142144, 2021.
- Guo, H.Y., Liu, J.M., Froyd, K.D., Roberts, J.M., Veres, P.R., Hayes, P.L., Jimenez, J.L., Nenes, A., and Weber, R.J.: Fine particle pH and gas-particle phase partitioning of inorganic species in Pasadena, California, during the 2010 CalNex campaign, *Atmos. Chem. Phys.*, 17, 5703–5719, 2017.
- Guo, H.Y., Otjes, R., Schlag, P., Kiendler-Scharr, A., Nenes, A., and Weber, R.J.: Effectiveness of ammonia reduction on control of fine particle nitrate, *Atmos. Chem. Phys.*, 18, 12241–12256, 2018.
- Song, S.J., Gao, M., Xu, W.Q., Shao, J.Y., Shi, G.L., Wang, S.X., Wang, Y.X., Sun, Y.L., and McElroy, M.B.: Fine particle pH for Beijing winter haze as inferred from different thermodynamic equilibrium models, *Atmos. Chem. Phys.*, 18, 7423–7438, 2018.

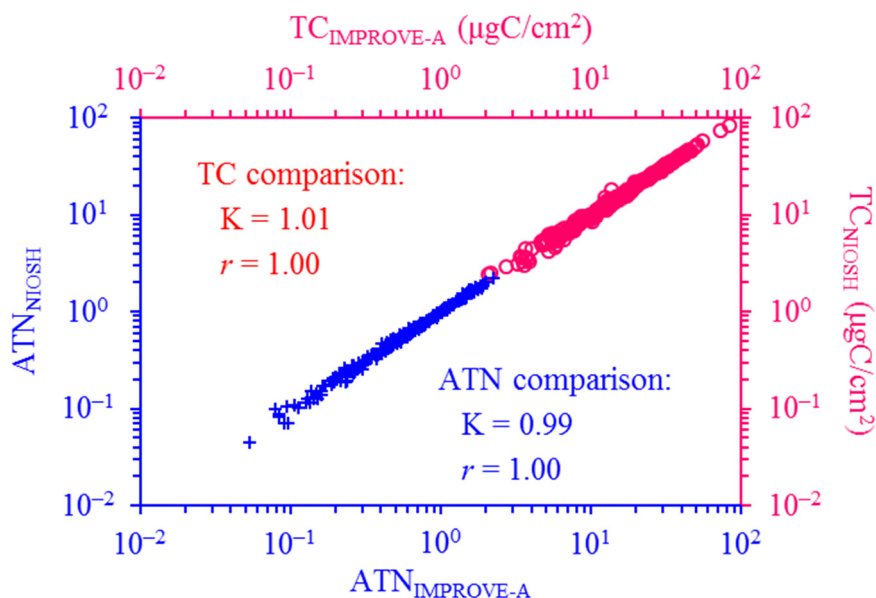


Figure S1. Comparisons of total carbon (TC) and optical attenuation (ATN) measured by different temperature protocols. Results from both campaigns are included. ATN is calculated as $\ln(I_{\text{final}}/I_{\text{initial}})$, where I_{initial} and I_{final} indicate filter transmittance signals measured at the beginning (i.e., when the loaded filter has not been heated) and end (i.e., when all the deposited carbon has been combusted off the filter) of thermal-optical analysis, respectively. Linear regression results are shown with K as slope (intercept was set as zero). TC and ATN agreed well between different protocols, demonstrating good precisions for both the carbon and transmittance measurements.

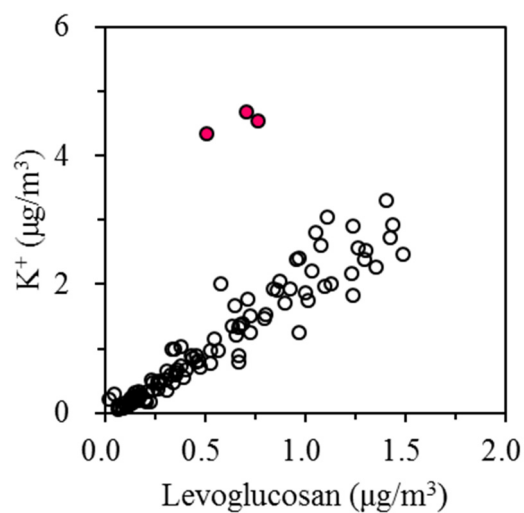


Figure S2. Relationship between K^+ and levoglucosan during the 2019–2020 campaign. Three samples collected during the Chinese New Year period exhibit substantially higher K^+ to levoglucosan ratios (as highlighted by the solid circles), pointing to significant influence of firework emissions.

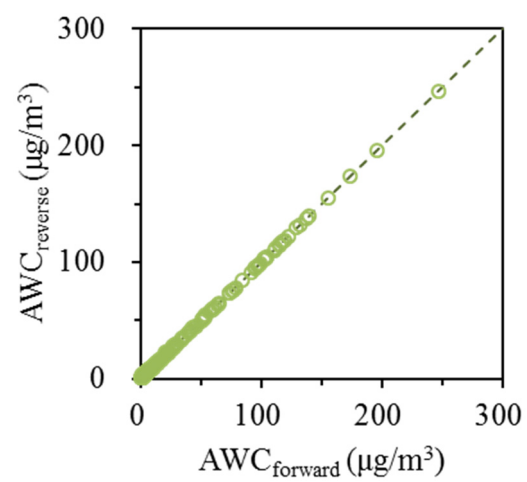


Figure S3. Comparison of AWC results predicted by reverse and forward modes. The dashed line indicates one-to-one correspondence.

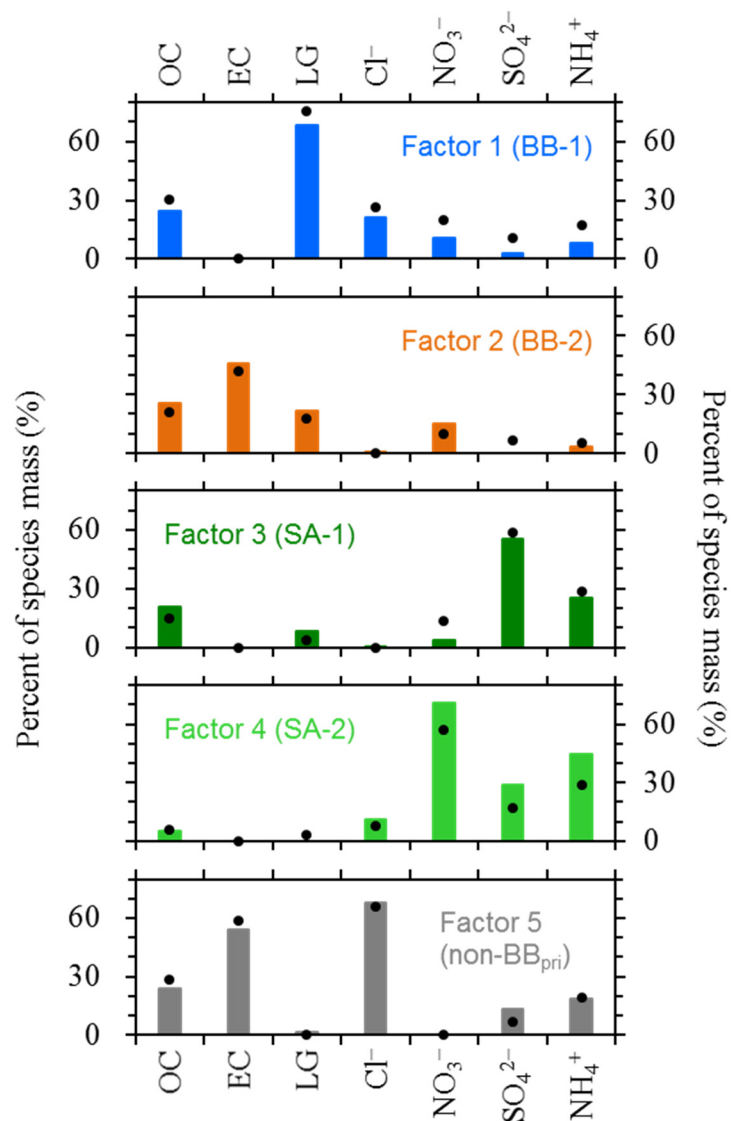


Figure S4. Source profiles resolved by PMF. The solid bars and circles indicate results obtained by this study and Cheng et al. (2021a), respectively. For this study, aerosol compositions measured during the 2018–2019 and 2019–2020 campaigns were combined and used as the PMF inputs, whereas Cheng et al. (2021a) was based only on the former campaign. In general, similar profiles were resolved by the two studies, despite the different measurement periods covered.

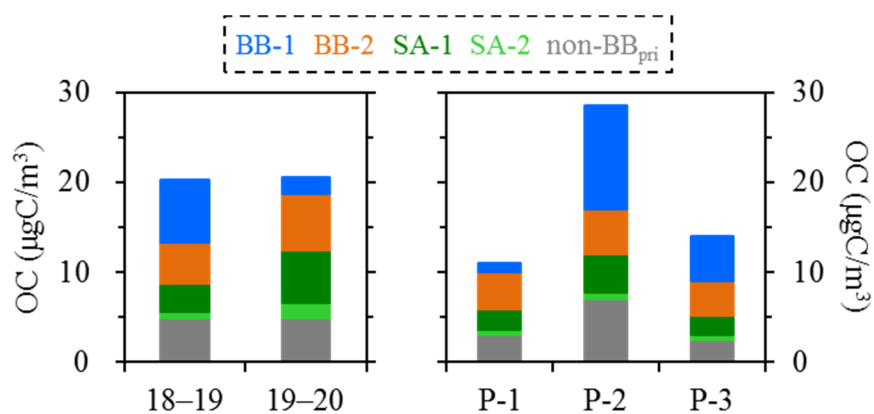


Figure S5. Comparisons of OC source apportionment results between the 2018–2019 and 2019–2020 campaigns (left panel), and across the 2018–2019 samples collected before (P-1), during (P-2) and after (P-3) the “legitimate burning” periods (right panel).

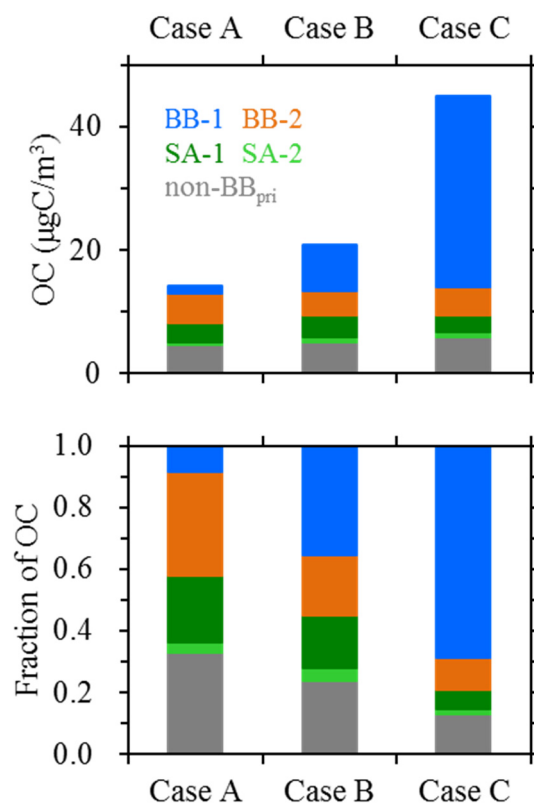


Figure S6. Comparison of OC source apportionment results across the 2018–2019 samples with increasing ~~strength~~ strengths of biomass burning ~~impacts~~ impact. Cases A, B and C correspond to LG/OC ranges of < 1.5%, 1.5–3.0% and > 3.0%, respectively.

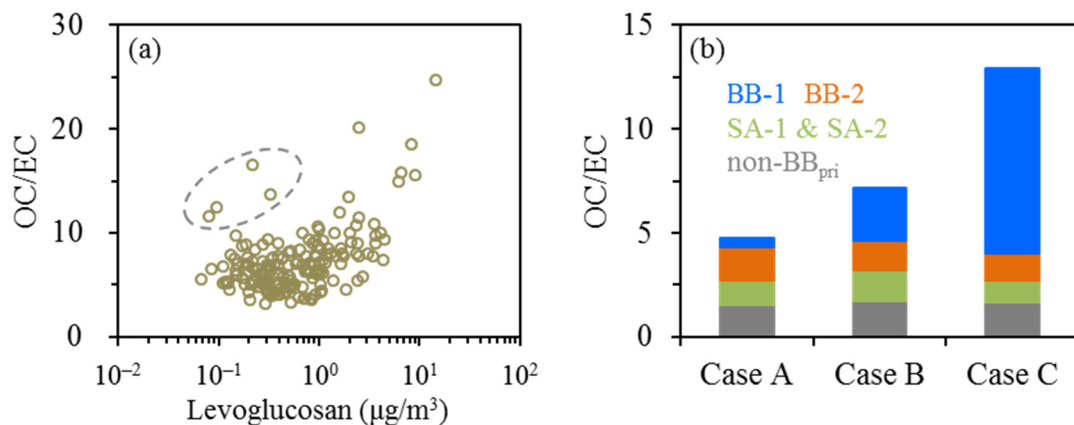


Figure S7. (a) Relationship between OC/EC and levoglucosan, and **(b)** comparison of OC/EC among Cases A–C, for the 2018–2019 campaign. OC/EC ratios in (b) are based on results from PMF analysis, i.e., for each case, OC/EC is presented as the sum of source-resolved OC to total EC ratios (e.g., $\text{OC}_{\text{BB-1}}/\text{EC}$ and $\text{OC}_{\text{BB-2}}/\text{EC}$). The two factors representing secondary aerosols are not distinguished in (b). In general, OC/EC showed a positive dependence on levoglucosan, although there appeared to be several outliers (as highlighted by the dashed oval) which had the lowest EC concentrations of the measurement period (below $\sim 0.5 \mu\text{g}/\text{m}^3$). Thus, biomass burning is considered the dominant driver for the temporal variation of OC/EC during the 2018–2019 campaign. This inference is also supported by (b), as OC/EC exhibited an increasing trend from Case A through Case C, which cannot be explained by SOA or non-BB emissions.

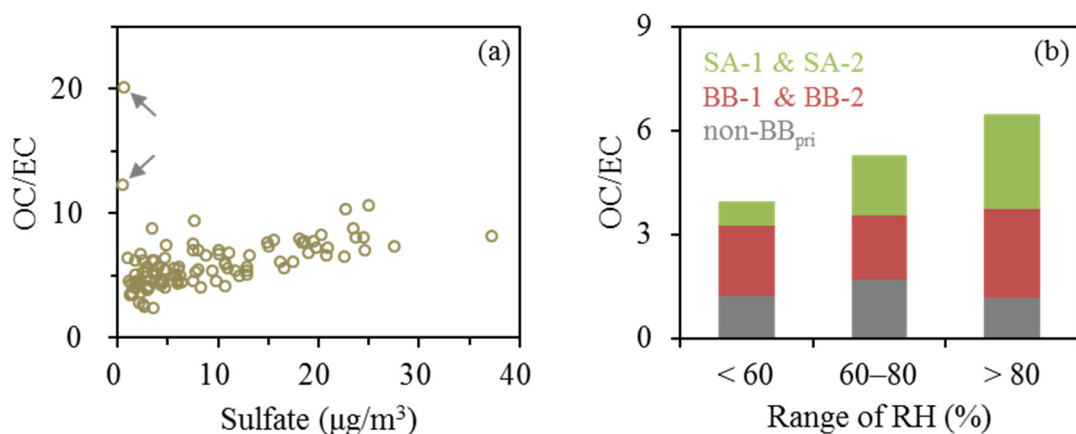


Figure S8. (a) Relationship between OC/EC and sulfate, and (b) comparison of OC/EC with increasing RH levels, for the 2019–2020 campaign. In general, OC/EC showed a positive dependence on sulfate, although there were two outliers (as highlighted by the arrows) which had the lowest EC concentrations of the measurement period (below $0.3 \mu\text{g}/\text{m}^3$). Thus, SOA is considered the dominant driver for the temporal variation of OC/EC during the 2019–2020 campaign. This inference is also supported by (b), as with increasing RH, OC/EC exhibited an increasing trend, which cannot be explained by the primary factors (either BB or non-BB).

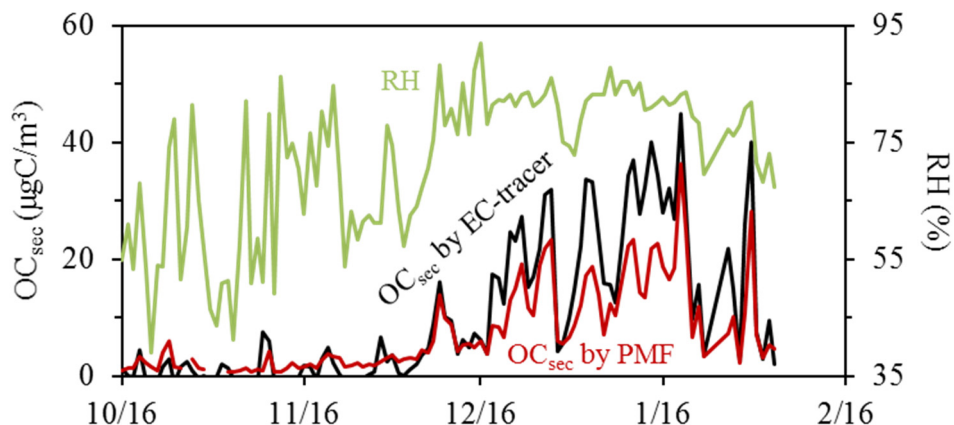


Figure S9. Temporal variations of OC_{sec} and RH during the 2019–2020 campaign. The PMF-based OC_{sec} was calculated as the sum of OC masses attributed to the SA-1 and SA-2 factors. For the EC-tracer method, OC_{sec} was calculated as: $OC_{sec} = OC - EC \times (OC/EC)_{pri} - OC^*$, where $(OC/EC)_{pri}$ is the OC to EC ratio representative of combustion sources and OC^* indicates primary OC from non-combustion sources. ~~For the 2019–2020 campaign, $(OC/EC)_{pri}$ and OC^* were determined as the slope (2.13) and intercept (3.11) from the linear regression of OC on EC ($r = 0.98$), respectively, based on the low RH samples (i.e., those with RH below 60%).~~ For the 2019–2020 campaign, $(OC/EC)_{pri}$ and OC^* were determined based on linear regression of OC on EC ($r = 0.98$), with $(OC/EC)_{pri}$ as the slope (2.13) and OC^* as the intercept (3.11), respectively, using low-RH samples (i.e., those with RH below 60%). Compared to the PMF-based results, OC_{sec} calculated by the EC-tracer method showed a similar pattern of temporal variation. Results from both methods showed RH-dependent increase of OC_{sec} .

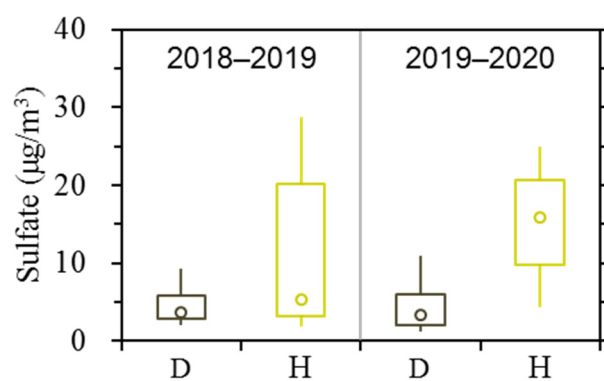


Figure S10. Comparison of sulfate between different RH levels for the 2018–2019 and 2019–2020 campaigns. The terms “D” and “H” indicate relatively dry and more humid conditions with RH below and above 80%, respectively.

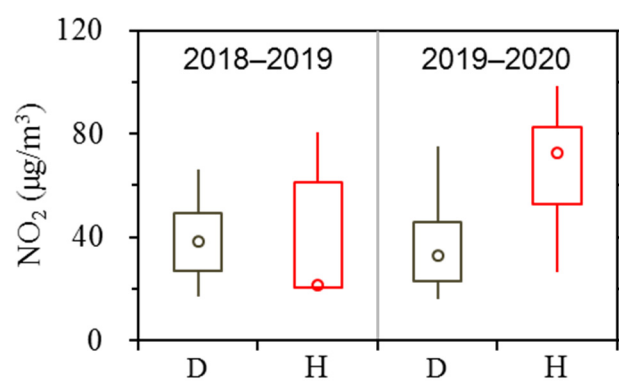


Figure S11. Comparison of NO₂ between different RH levels for the 2018–2019 and 2019–2020 campaigns. ~~The terms “D” and “H” indicate relatively dry and more humid conditions with RH below and above 80%, respectively.~~

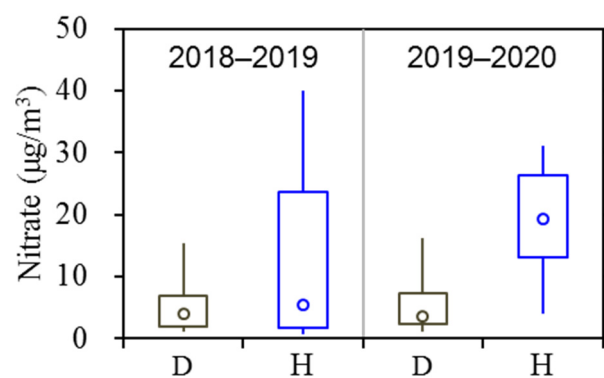


Figure S12. Comparison of nitrate between different RH levels for the 2018–2019 and 2019–2020 campaigns. ~~The terms “D” and “H” indicate relatively dry and more humid conditions with RH below and above 80%, respectively.~~

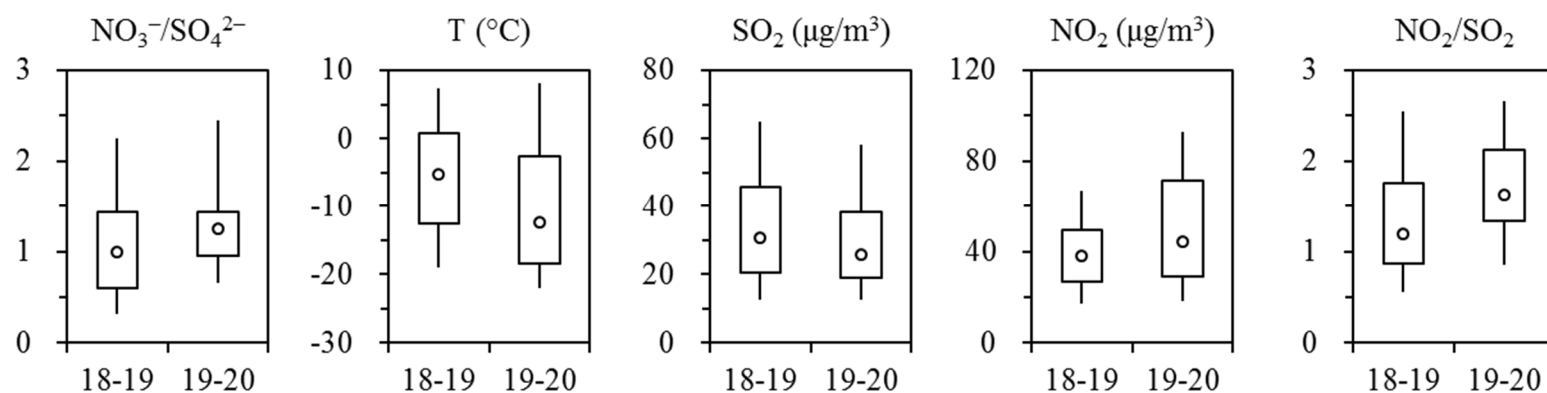


Figure S13. Comparisons of the nitrate to sulfate ratios, ~~temperature~~ temperatures, SO_2 , NO_2 and the NO_2 to SO_2 ratios between the 2018–2019 and 2019–2020 campaigns.

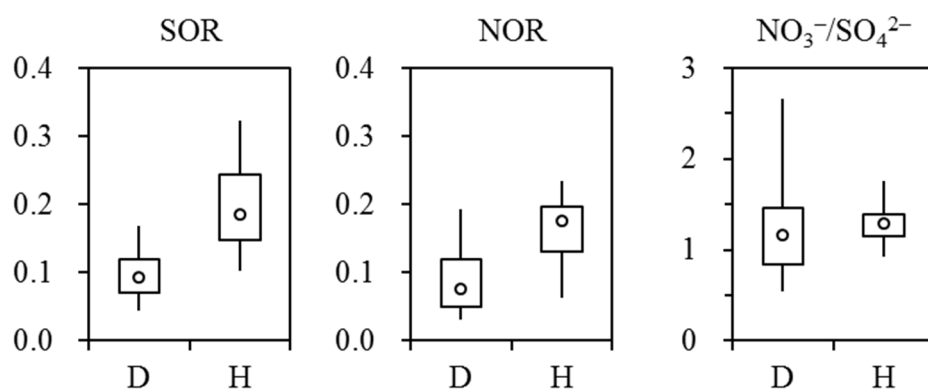


Figure S14. Comparisons of SOR, NOR and the nitrate to sulfate ratios at different RH levels for the 2019–2020 campaign.

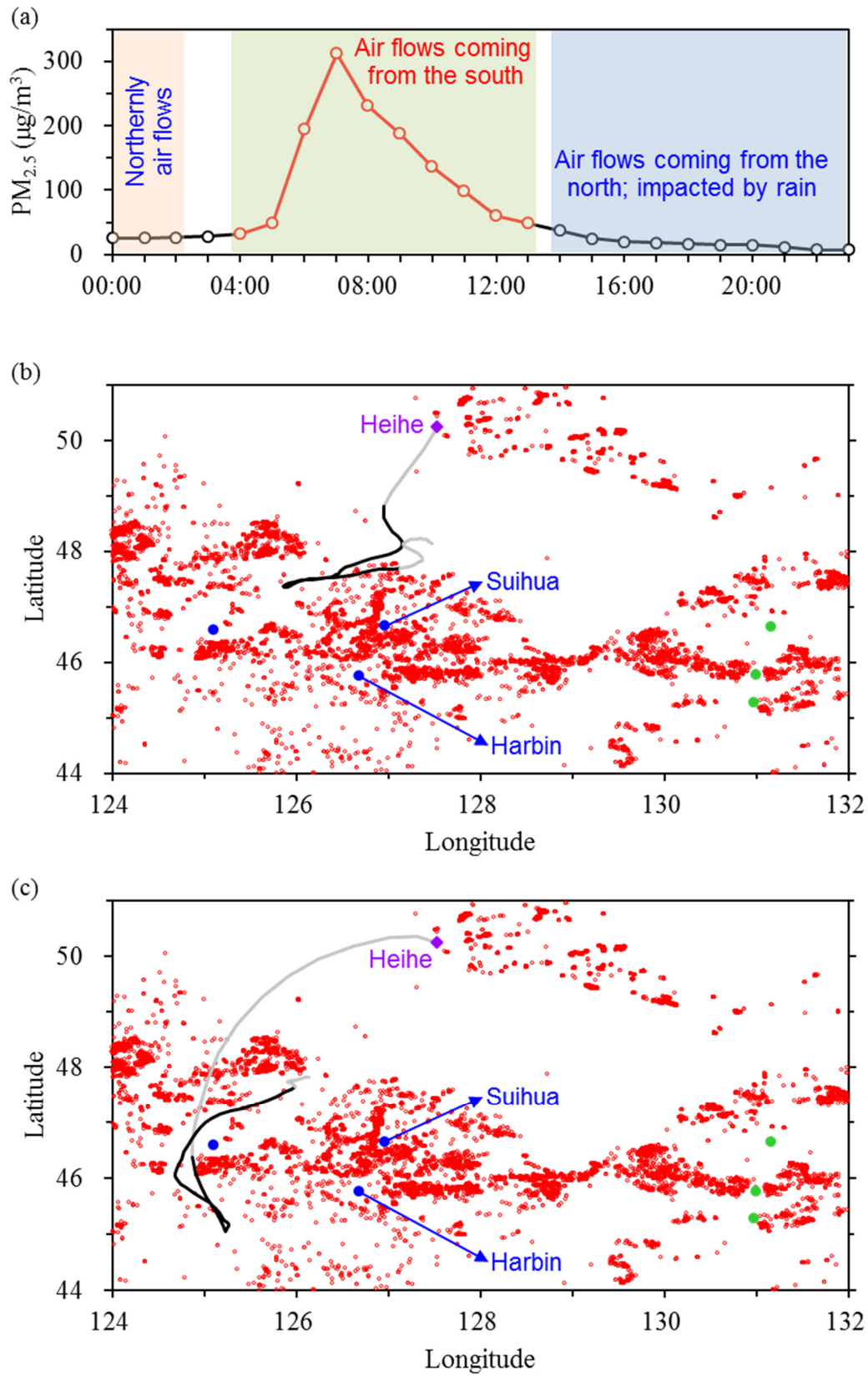


Figure S15. (a) Temporal variation of 1-h $PM_{2.5}$ observed in Heihe on 19 April, 2020. (b–c) 72-hour back trajectories ending at 4:00 and 13:00, respectively, in Heihe, overlaid with active fires detected during 17–18 April, 2020 as red circles. $PM_{2.5}$ were relatively low between 0:00 and 3:00,

when the air flows came from the northwest, moved fast and descended sharply. $PM_{2.5}$ started to increase at 4:00, with the trajectory from the south and impacted by the region with agricultural fires (as shown in b). The increase of $PM_{2.5}$ continued as the trajectory path moved towards Harbin and Suihua, where the impacts of open burning were inferred to be extremely strong based on their off-the-chart $PM_{2.5}$ concentrations. The maximum $PM_{2.5}$ was observed at 7:00, and then $PM_{2.5}$ started to decrease although the air masses still passed over the Harbin-Suihua region (or the nearby area) before arriving at Heihe. A likely cause for the decrease of $PM_{2.5}$ after 7:00 was the increase of planetary boundary layer height from morning through noon time. The trajectory left the Harbin-Suihua region at 13:00 (as shown in c) and returned to the north at 14:00. In addition, there was rain in Heihe after 14:00, and correspondingly, $PM_{2.5}$ gradually decreased to below $10 \mu\text{g}/\text{m}^3$.